NTNU
Norwegian University of
Science and Technology

Karlsruhe Institute of Technology

Magnon dispersion relation in ultrathin Co films grown on Ir(111)

Master Thesis

of

Andrea Hjelt

A thesis submitted in fulfillment of the requirements
for the degree of Master of Physics

in the

Heisenberg Spin-dynamics Group
Physikalisches Institut (PHI)

September 2, 2019

Reviewer:
PD Dr. Khalil Zakeri Lori

2nd Reviewer:
Prof. Dr. Matthieu Le Tacon

Ich erkläre hiermit, dass ich diese Arbeit selbstständig verfasst und keine anderen als die angegebenen Quellen und Hilfsmittel verwendet habe. Die wörtlich oder inhaltlich übernommenen Stellen habe ich als solche kenntlich gemacht. Die Regeln des Karlsruher Instituts für Technologie zur Sicherung guter wissenschaftlicher Praxis in der Fassung vom Mai 2018 habe ich beachtet.

Karlsruhe, 1. September 2019

"*Probleme kann man niemals mit derselben Denkweise lösen,*
durch die sie entstanden sind."

Albert Einstein (1879-1955)

Abstract

In this work the magnetic properties of a 1.6 ML Co film grown on an Ir(111) substrate were investigated using spin-polarized electron energy loss spectroscopy (SPEELS). Two magnon excitation peaks were identified, and their dispersion relation was measured along the $\bar{\Gamma}$-$\bar{\mathrm{K}}$-direction of the surface Brillouin zone. A careful analysis of the two magnon peaks revealed that they originate from a complex surface with trilayer patches. The first excitation peak was identified to originate from the $n = 0$ magnon mode of a trilayer structure. The second excitation peak could either originate from the $n = 0$ magnon mode of bilayer patches, or from the $n = 1$ magnon mode of trilayer patches. It was concluded that the Co film grows in a Vollmer-Weber manner. Measurements have been conducted with the aim to quantify the effects of the DM-interaction on the magnon dispersion relation. Our measurements showed a slight effect, but the broadening of the magnon peaks made it hard to quantify this interaction. The system has successfully been modelled by first-principles calculations, taking into account the correlation effects. The exchange constants were estimated to be $J_{\parallel}^{i} = 4.8\,\mathrm{meV}$, $J_{\parallel}^{m} = 6\,\mathrm{meV}$ and $J_{\parallel}^{s} = 8.2\,\mathrm{meV}$, where $J_{\parallel}^{i}$, $J_{\parallel}^{m}$ and $J_{\parallel}^{s}$ represent the values of the intralayer exchange constants in the interface, middle and surface layer, respectively. For interlayer exchange, the exchange constants were estimated to be $J_{\perp} = 5.2\,\mathrm{meV}$ for exchange between the interface and middle layer, and $J_{\perp} = 11.8\,\mathrm{meV}$ for exchange between the middle and surface layer.

Contents

List of Abbreviations

SPEELS	**S**pin **P**olarized **E**lectron **E**energy **L**oss **S**pectroscopy
HV	**H**igh **V**oltage
UHV	**U**ltra **H**igh **V**acuum
MOKE	**M**agneto **O**ptic **K**err **E**ffect
AES	**A**uger **E**lectron **S**pectroscopy
LEED	**L**ow **E**nergy **E**lectron **L**oss **S**pectroscopy
LC	**L**eft **C**ircular (polarization)
RC	**R**ight **C**ircular (polarization)
RHEED	**R**eflection **H**igh **E**nergy **E**lectron **D**iffraction
ML	**M**ono **L**ayer
STM	**S**canning **T**unneling **M**icroscopy

Chapter 1

Introduction

Magnetism is an exciting phenomena that has been known, and studied, since ancient times. The word "magnet" comes from old Greek and means "stone from Magnesia" [1]. The first definite statement on magnetism is attributed to Thales of Miletus (approx. 634-546 BC) who said that lodestone attracts iron [2]. The invention of the compass is perhaps the first practical application of magnetism. The use of the compass for navigation represented an important progress in human abilities. The first scientific publication on magnetism is the book "De magnete" by William Gilbet, published 1600 in London. In this book he proposed that the Earth itself is a giant magnet. The field of the Earth was modeled in detail around 1835 by Carl Friedrich Gauss (1777-1855) [2]. In 1819 Hans Christian Ørsted (1777-1851) observed that a magnetic force is exerted on a magnetic needle by the electric current in a nearby wire, leading to the discovery of electromagnetism [3]. This represented a revolution in our understanding of magnetism as well as our practical applications of it. Electromagnetism was thoroughly studied throughout the 19th century by scientists like Jean-Baptiste Biot (1774-1861), Felix Savart (1791-1841), André Mairue Ampère (1775-1836), Michael Faraday (1791-1867) and James Clerk Maxwell (1831-1879) [4–6]. The next big revolution came during the 21st century, with the establishment of quantum theory [7–11]. Within this framework, the underlying mechanisms leading to magnetism can be understood.

In parallel with the development of our understanding of magnetism, new technological equipment were invented that have revolutionized our societies. Today, in our modern civilization, the utilization of magnetism is of crucial importance. The modern world is completely reliant on electricity, wireless communication at the speed of light and high-tech magnetic devices used in information technology. Since the very beginning of computer science, magnetism was utilized for memory recording in devices like hard drives and the old fashioned floppy disk. Computers today, are still reliant on magnetic recording, but getting access to the recorded data is not as

efficient as it could be. A potential new technology that could utilize bosonic quasi-particles for information processing, would be expected to generate both faster and more energy efficient devices [12–14].

Magnons are bosonic quasi-particles that refer to the collective modes of spin excitations in a magnetic solid. They play an essential role in many observed magnetic phenomena and represent a very interesting field of study, that lies at the heart of condensed matter physics. Magnons in ultrathin ferromagnetic films, with thickness of a few atomic layers, are of particular interest, both for potential utilization in new technologies and from a physical point of view. In ultrathin films one can fabricate the system to investigate specific effects and geometries that would be possible to observe in nature. The vertical constraint of such a film allows only for short-wavelength magnon modes. The number of confined magnon modes is equal to the number of atomic layers [15]. The presence of the vacuum-film and substrate-film interfaces influences the bonding environment for the atoms in each layer. The differences in bonding environment leads to distinctive magnon states, each with their own characteristics [16]. Modifications to the exchange interaction that for example can be imposed by adjustments of the lattice strain, the atomic structure and the film substrate are possible tools to engineer these magnon modes.

In this thesis 1.6 monolayers (ML) of Co grown on an Ir(111)-substrate is investigated. Here, "atomic monolayer" (ML) refers to a single atomic layer of the material. The system is of great interest, because a quantitative understanding of the dispersion relation of Co films grown on different surfaces is not yet available. Earlier research has found that first-principles calculations within the generalized gradient approximation of the density functional theory (DFT) are efficient for predicting magnon energies for Fe systems [16–18]. A study where the magnon dispersion relations were measured for different Co systems revealed that the first-principles calculations heavily overestimate the magnon energies of the films [19]. A better agreement with the experimental results was found by a renormalization of the majority-spin states of the 3d bands towards the Fermi level while keeping the minority-spin states unchanged [20–22]. However, it was, necessary to explain the experimental data from the Co film grown on a Pt(111)-surface with a stronger renormalization compared with the Ir(001) and Cu(001) surfaces. The answer to this question, whether the (111)-surface in general requires a stronger renormalization of the majority bands remains unclear. The Ir(111) substrate is chosen to provide further insights on this matter. Moreover, Ir is a heavy metal and exhibits a large

spin-orbit coupling. It is therefore expected that it is possible to measure the antisymmetric Dzyaloshiniskii-Moriya-exchange-interaction (DM-interaction) for this substrate [23–26]. This is also an interesting topic, that has not yet been investigated.

A brief theoretical introduction to the specific topics discussed in this thesis is given in Chapter 2. The chapter also includes an introduction to the Dzyaloshiniskii-Moriya-exchange-interaction mentioned above. The dispersion relation of a bilayer and trilayer fcc(111)-system is calculated by a simple Heisenberg model in Section 2.4. Chapter 3 provides an introduction to the SPEELS lab and a calibration calculation for the deposition of Co. The results are presented and discussed in Chapter 4. The measured dispersion relation is compared with calculations in Section 4.3 of this chapter. Chapter 5 provides a short summary and the conclusions that have been drawn from this work.

Chapter 2

Theoretical Background

2.1 Long range magnetic order

The Bohr van Leeuwen theorem states that when statistical mechanics and classical mechanics are applied consistently, the thermal average of the magnetization is always zero [27]. As a consequence, magnetization is a purely quantum phenomena. In quantum theory, permanent magnetization is caused by the alignment of electron spin in the material. On an atomic scale, electrons in the same orbital prefers to have their spin parallel in accordance with Hund's 1st rule [28]. This is due to the Coulomb interaction between the electrons and the charged nucleus [29]. The closer the electrons are to each other in space, the more efficiently they screen the nuclear charge and the weaker they are bound to the nucleus. The Coulomb energy is minimized when the electrons are in an antisymmetric spatial state, and thus a symmetric spin state, because this maximize the distance between them and thus minimize the screening of the nuclear charge. The most well known magnetic materials are of the 3d-transition metals, such as Mn, Fe, Co and Ni. These are materials that all have a total spin magnetic moment on an atomic scale due to their spin configuration, the electron orbits and spin-orbit effects. The electron configuration of Co, which is studied in this paper, is $[Ar]3d^74s^2$. The spin configuration is shown in Fig. (2.1). In sum the Co has three spin up that contribute to the magnetization. The magnetic moments of the transition metals are almost entirely due to the d-electrons [2]. It is, however, important to note that because they are metals, the atoms are coupled together through metallic bonds. Some of the electrons are therefore itinerant and the isolated atomic picture is incorrect. Rather than single

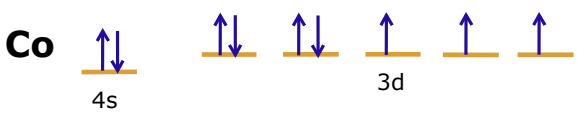

FIGURE 2.1: The spin configuration of Co, that has electron configuration $[Ar]3d^74s^2$

.

isolated atoms, one may consider each lattice point in the metallic crystal as a carrier of a magnetic moment. For long range magnetism, the magnetization of these lattice sites must prefer to align. One may consider each lattice site, i, to have net magnetic moment μ_i. The interactions between the sites are determining the long range order of the system. The spins themselves produce a dipolar magnetic field and may interact through a dipole-dipole interaction. This interaction is, however, too weak to explain magnetic order at temperatures above 1 K [27]. The strongest long-range interaction between spins, and the main reason for magnetic order above 1 K, is the exchange interaction. The exchange interaction origins from the energy required to change quantum states between two electrons. The joint wavefunction of two electrons may be a singlet of total spin 0 and energy E_S, or a triplet of total spin 1 and energy E_T. The energy associated with an exchange from a singlet to a triplet state defines the exchange constant

$$2J = E_S - E_T. \tag{2.1}$$

In a microscopic description of a macroscopic magnetic system, the exchange interaction may be described by the Heisenberg Hamiltonian [30, 31]

$$\mathcal{H}_{Ex} = -\sum_{ij} J_{ij}\mathbf{S}_i \cdot \mathbf{S}_j, \tag{2.2}$$

where J_{ij} is the exchange constant between the i^{th} and j^{th} spins. If J is positive, $E_s > E_T$ the spins prefer to align parallel. If J is negative, $E_s < E_T$ and the spins prefer to be antiparallel. Even though the exchange interaction is responsible for long range magnetic order it does require an overlap of the electron wavefunctions. It is therefore a strong, but short-ranged, interaction. The Heisenberg Hamiltonian is symmetric on the behalf of spin exchange and does not discriminate between the spatial directions in which the spins may be parallel or anti-parallel. Real ferromagnets, however, often have a preferred axis of magnetization. The magnetic anisotropy is defined as the energy that it takes to rotate the magnetization direction from the easy (preferred) into the hard direction. The main contributor to the magnetic anisotropy is the spin-orbit interaction. The magnetic anisotropy couples the spin to the crystal lattice [2]. In comparison to the Heisenberg exchange interaction, this effect is weak. In some arrangements the exchange coupling also has an antisymmetric component, that also origins from spin-orbit coupling. The so-called Dzyaloshiniskii-Moriya (DM) interaction act between two spins $\mathbf{S_1}$ and $\mathbf{S_2}$ and has the Hamiltonian

$$\mathcal{H}_{DM} = -\sum_{\mathrm{ij}} \vec{D}_{ij} \cdot \mathbf{S}_\mathrm{i} \times \mathbf{S}_\mathrm{j}, \tag{2.3}$$

where $\vec{\mathrm{D}}_{ij}$ is the Dzyaloshiniskii-Moriya vector [23–26]. The lowest DM-energy is obtained when the spins are at right angles to each other in a plane perpendicular to the DM-vector. The DM interaction is much weaker than the Heisenberg interaction and varnishes for systems with inversion symmetry. In systems with broken inversion symmetry, its most common effect is to rotate the spins by a small angle. An ultrathin surface of a magnetic material often has a broken symmetry and therefore also a DM-contribution to its Hamiltonian. From Eq. (2.3), one can show that the dispersion relation of this DM-term, considering only the nearest neighbor interactions can be written as

$$E_{DM} = c \ \sin^2\theta \sum_{\mathbf{R}} \left(\mathbf{D}_1 \cdot \hat{\mathbf{e}}\right) \sin(\mathbf{q} \cdot \mathbf{R}). \tag{2.4}$$

Here c is the chirality rotation index (+1 for right rotating sense and -1 for left), θ denotes the relative angle between the neighboring spins, D_1 is the DM vector of the nearest neighbors, $\hat{\mathrm{e}}$ denotes the direction of the easy axis and R represent the position vector of nearest neighbors [32]. From this equation one expects a sinusoidal behaviour of the energy shift due to the DM interaction, as a function of wavevector q. In summary, the total Hamiltonian for a spin system may be written

$$\mathcal{H} = \mathcal{H}_B + \mathcal{H}_{Ex} + \mathcal{H}_{DM} \tag{2.5}$$

where $\mathcal{H}_B$ describes the response of the system to an external magnetic field and $\mathcal{H}_{Ex}$ and $\mathcal{H}_{DM}$ are defined by Eq.(2.2) and Eq.(2.3) respectively.

2.2 Magnetic excitations

In a perfect ferromagnet at 0 K, all the electron spins that contribute to the magnetization are parallel. A possible excitation in such a system is the spin flip of an electron. A spin flip from $\mathrm{S} = \hbar/2$ to $\mathrm{S} = -\hbar/2$ requires a change in spin angular momentum of $\Delta\mathrm{S} = 1\hbar$. Such a spin flip excitation can be shared by many electrons and is referred to as a magnon. A magnon is a quasi-particle which carries a total angular momentum of $\mathrm{S} = 1\hbar$ and is thus a Boson. The energy of the magnon depends on how localized the spin excitation is. There are two main pictures describing the spin excitation, that are suited for each their energy range. The Stoner model describes an itinerant band-model that is suitable for high-energy magnon

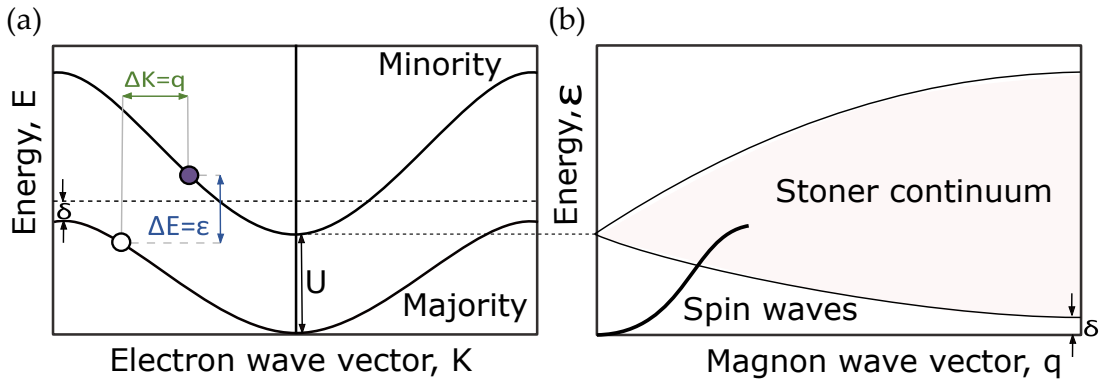

FIGURE 2.2: **(a)** Exchange split bands according to the Stoner model. The majority band lies under the Fermi energy E_F, by an amount δ. The exchange energy separating the two bands is marked by U and is here constant across the Brillouin zone. As an electron from the Majority band is excited to the Minority band, a hole is created in the Majority band. Due to the spin flip, the electron hole pair has angular momentum $1\hbar$ and may be referred to as a magnon. The magnon momentum $\mathbf{q} = \Delta K$ is marked by the green arrow. The energy of the magnon ϵ is marked by the blue arrow. **(b)** The magnon energy as a function of wave vector, q. The gray region mark the Stoner continuum, the allowed energies for Stoner excitations according to the band shown in (a). Note that the energy of a Stoner excitation with wave vector $\mathbf{q} = 0$, corresponds to the exchange energy U. The Spin wave line represents the energy dispersion for low energy magnons. They can be seen as spin waves or bound excitation states according to the picture in (a). Bound excitations are however not part of the Stoner model, that only considers non-interacting electron-hole excitations. Figure inspired from [32].

excitations [33–35]. The spin wave model describes a picture in which the magnon is shared by many lattice sites in the crystal and therefore the energy may be very low [36–39]. The Stoner model is discussed in subsection 2.2.1 and the spin wave picture is discussed in subsection 2.2.2.

2.2.1 Stoner excitations

The Stoner model takes into consideration that most permanent magnetic materials are metals and that therefore, some of the carriers of magnetic moments are conduction electrons that must be considered as freely moving in a periodic potential. This leads to a band model in which the electrons are located in k-space rather than at particular positions in the crystal. Magnetism is in the Stoner model explained by an energy shift between the band containing spin up states and the band containing spin down states. A ferromagnet has the majority of its spins pointing in the direction opposite to the magnetic field. (Electrons are particles of negative charge and has magnetic moment in the opposite direction as the angular momentum, thus spin.) Defining spin up to be the spin antiparallel to the magnetic field, the majority band in a ferromagnet consists of states with spin up and the minority band consists

of states with spin down (this notation is the convention used the SPEELS-society). Fig. 2.2(a) illustrates the Stoner bands for a strong ferromagnet. The exchange energy discussed in Section 2.1 is here represented by the term U, that is the energy shift between the bands and is here assumed to be a constant throughout the Brillouin zone. The majority band lies below the Fermi energy E_F by an amount δ, and is thus completely filled. The minority band is only partially filled. This leads to a net magnetization of the material, as there are more spin up than spin down. As temperature rise some electrons in the majority band may get thermally excited and jump up to the minority band, leaving a hole behind. This weakens the net magnetization and at sufficiently high temperatures the spontaneous magnetization is completely broken. The Stoner model can therefore give predictions about the Curie temperature of a material but the predictions are heavily over estimated [2] because only high energy magnon excitations are considered by the model. The only excitation considered in the Stoner model, the so-called Stoner excitation, is an magnon exciton with zero correlation between the excited electron and hole. There are therefore no lower energy, bound, magnon exciton states in the Stoner picture. Additionally the excitation requires that the excited electron undergoes a full spin flip, changing its spin angular momentum by $1\hbar$, at the cost of the full exchange energy of each surrounding neighbor. Lower energy excitations are possible when the spin flip is shared by many electrons. The spin wave picture is made to describe the lowest energy excitations in a spin system, and complements the Stoner model. The energy dispersion of the two models are sketched in Fig.2.2(b). It can be seen that the discrete spin wave energies merge with the energies of the Stoner excitations, referred to as the Stoner continuum. For a Stoner excitation, the magnon wavevector, $\mathbf{q}$, is given by the green arrow in Fig.2.2(a). The excitation energy, ϵ, is given by the blue arrow. By moving the Stoner excitation in Fig.2.2(a) across the Brillouin zone it can be easily seen that the energies, ϵ, establish a continuum. At zero magnon wavevector the excitation costs energy $\delta\epsilon = \mathrm{U}$ and at high magnon wavevector the excitation energy is $\delta\epsilon = \delta$.

2.2.2 Spin Waves

The spin wave model considers the lowest energy excitations of a spin system. They are, opposed to the Stoner excitations, of collective nature. In a Stoner excitation, the excited electron undergoes a full spin-flip transition. The spin wave excitation share the spin reversal coherently over the whole crystal. In a semi-classical picture the spin wave excitation may be considered as a distortion of the Larmor precession

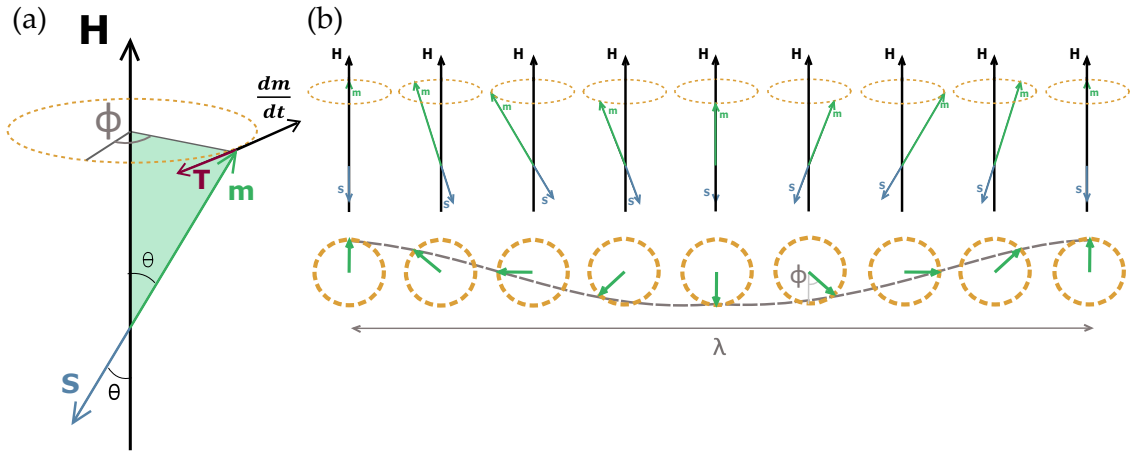

FIGURE 2.3: **(a)** Larmor precession of the spin and magnetic moment of an electron. The magnetic moment, m, experiences a torque, T, that causes m to move in the opposite direction of the torque and thus precess around H rather than align to it. This comes from the fact that the electron has a spin angular momentum that the torque acts to change according to Equations 2.8 and 2.9. **(b)** A spin wave in the semi-classical picture. As the spin flip is shared by many electrons, it cause an out of phase precession of the magnetic moments, m. The wavelength of the spin wave is illustrated in the lower part of the figure.

about the local exchange field across the crystal. Fig. 2.3(a) illustrates, semi-classically, how the magnetic moment and spin of an electron precess about a H-field. The magnetic moment, $\vec{m}$, of an electron, points in the opposite direction of its spin angular momentum, $\vec{S}$, due to the fact that electrons are negatively charged particles. The moment, $\vec{m}$, experiences a torque:

$$\vec{\tau} = \vec{\mathrm{m}} \times \vec{\mathrm{H}}, \tag{2.6}$$

that tends to rotate $\vec{\mathrm{m}}$ to align parallel with $\vec{\mathrm{H}}$. The electron does, however, have angular momentum in the direction of the spin and the magnetic torque will change the direction of the angular momentum, forcing the spin to precess about $\vec{\mathrm{H}}$, rather than to align to it. This can be easily derived from Newton's 2nd law for rotational motion:

$$\vec{\tau} = \frac{d\vec{\mathrm{L}}}{d\mathrm{t}}. \tag{2.7}$$

The magnetic moment of the electron is given by the angular momentum as:

$$\vec{m} = -\gamma\vec{\mathrm{L}} \tag{2.8}$$

with $\gamma = g\mu_B/\hbar$, where g is the g-factor and $\mu_B = e\hbar/2m_e$ is the Bohr magneton [2]. Substituting Equation 2.6 and 2.8 into Equation 2.7 gives an expression for the precession of the magnetic moment, $\vec{\mathrm{m}}$:

$$\frac{d\vec{\mathrm{m}}}{dt} = -\gamma[\vec{\mathrm{m}} \times \vec{\mathrm{H}}] = -\gamma\vec{\tau}. \tag{2.9}$$

As shown by Fig.2.3(a), the magnetic moment will move in the opposite direction as the magnetic torque. The lowest energy state of a spin system, is a state in which all spins are aligned, precessing coherently about the local exchange field H. If the spin of an electron as illustrated in Fig.2.3(a) is flipped slightly, it will cause the angle θ to change. A change in θ will cause a change in the torque, $\vec{\tau}$, as the torque is defined through Equation 2.6 as $\tau = mH\sin\theta$. The change in the torque will cause a change in $d\vec{\mathrm{m}}/dt$, that will make this electron precess slightly out of phase relative to the others. The coherence is broken. In this semi-classical picture, a spin wave is seen as such an out-of-phase precession of the spins. Fig. 2.3(b) provides an illustration of such a spin wave with phase shift ϕ. The longer the wavelength of the spin wave, the more electrons share the spin flip and the lower the energy of the excitation. The lowest energy spin waves have so large wavelength that the strong, short-ranged, exchange interaction is not as dominant and the the weak, long range, dipole-dipole interaction becomes important. This is the case for spin waves with wavevectors below q $< 10^{-3}$Å^{-1} [40]. For wavevectors above q $> 10^{-2}$Å^{-1} the exchange interaction is as good as the only interaction that determines the spin wave energy. The measurements in this thesis is well within the exchange interaction regime.

2.3 Ir(111) surface

Iridium is a metal with a face centered cubic (fcc) structure and lattice parameter $a_{Ir} = 3.839$ Å [41]. The fcc(111) surface is shown by the three figures in Fig. 2.4. Figure2.4(a) shows the fcc structure and the shaded region marks the (111)-surface. The blue color marks the lattice sites that are contributing to the shaded surface. In Fig. 2.4(b), consecutive (111)-surface layers are illustrated, each surface marked by a different color. Figure 2.4(c) is an illustration of the surfaces as seen from above. The top layer is marked by red, the layer beneath is marked by yellow, and the layer beneath the yellow layer is marked by blue. The surface is clearly hexagonal, and each layer is slightly shifted with respect to its neighboring layers. This is emphasized by the colored hexagons that clearly shift as one moves to another layer. A 4th layer would overlap with one of the layers already shown in the figure, as seen from above.

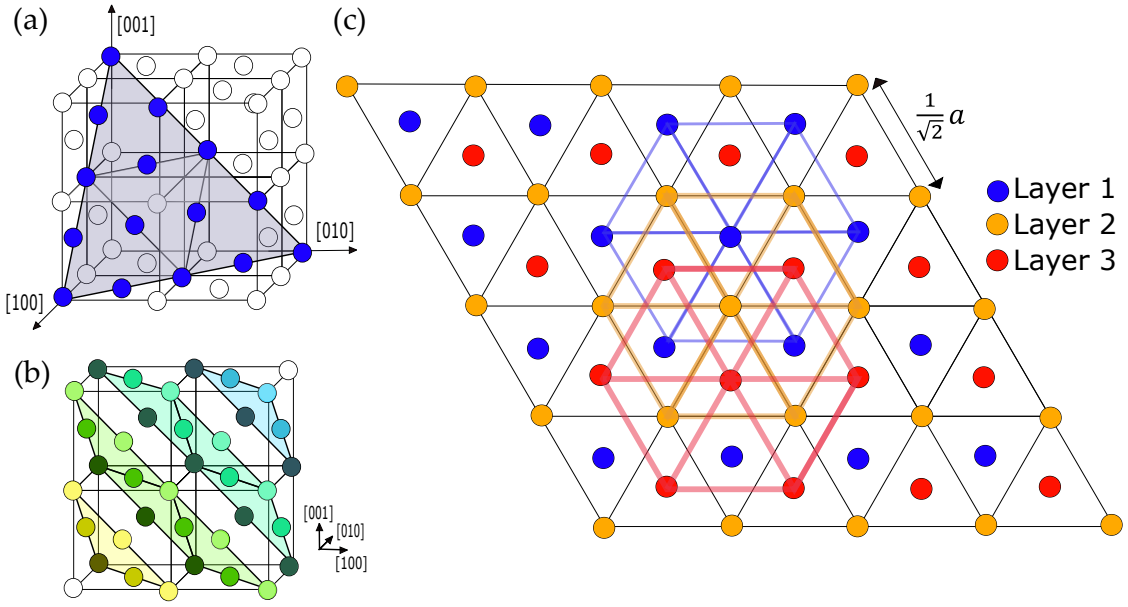

FIGURE 2.4: **(a)** The fcc structure with a (111)-surface marked by the shaded area. The blue, mark lattice sites that are at the surface. **(b)** Consecutive (111)-surfaces each marked by a different color. The interplanar distance is $d = a/\sqrt{3}$. **(c)** The fcc(111) surface as seen from above for three consecutive surface layers. The top layer is marked by red, the layer beneath is marked by yellow, and the layer beneath the yellow layer is marked by blue. Each layer is slightly shifted with respect to its neighbors, which is made clear by the colored hexagons.

2.3.1 Film growth

Epitaxy refers to the method of depositing a mono-crystalline film on a mono-crystalline substrate. The deposited film is denoted as epitaxial if it matches the crystalline order of the substrate. In the case of Frank-van der Merwe layer-by-layer growth, or Stranski-Krastanov layer-plus-island growth, the first atomic layer of an epitaxially grown film is perfectly aligned with the crystalline structure of the substrate. As more atomic layers are added, the film surface may deviate from the substrate surface and at some thickness the film structure is completely independent of the substrate [42]. The measurements in this thesis are of a 1.6 ML thick Co film grown on an Ir(111) surface. For 1 ML thickness the Co grow completely according to the crystalline structure of the Ir(111) substrate. Co has naturally a hexagonal close packed structure with lattice parameters $a_{Co} = 2.507$ Å [41] and $c > a$. The surface inter-atomic distance, d_{Ir}, of the Ir(111) surface is, as can be seen in Fig.2.4(c),

$$d_{Ir} = \frac{1}{\sqrt{2}} a_{Ir} \approx 2.7\text{Å}. \tag{2.10}$$

From this it is clear that the inter-atomic distance in basal plane of Co is smaller than the inter-atomic distance of the Ir(111)-surface; $a_{Co} < d_{Ir}$. The Co prefers to

maintain its volume density. To compensate for the larger lattice parameter when grown on the Ir-film, the inter-planar distance of the Co layers is less than the inter-planar distance in the Ir substrate. The film does not grow perfectly smooth. A 1.6 ML film consists of large patches of 2 ML, maybe even some small patches of 3 ML because the Co could prefer to complete the unit cell. It is known that for a Co film, ferromagnetic order is observed at film thicknesses above 1.3 ML [43]. It is therefore reasonable to assume that the magnon signal is originating from patches of 2 ML. A film of thickness 1.6 ML has sufficiently large areas covered by 2ML to ensure a good magnon signal and can be considered to be a 2 ML film when used for measuring magnons.

2.4 Spin waves in the Heisenberg model

The exchange interaction energy of two neighbouring electrons i and j, each with spin **S**, is described by the Heisenberg Hamiltonian:

$$\mathcal{H} = -\sum_{\mathrm{ij}} J_{ij}\mathbf{S}_{\mathrm{i}} \cdot \mathbf{S}_{\mathrm{j}} = -\sum_{\mathrm{ij}} J_{ij} \cdot \frac{\hbar^2}{4} \cdot \boldsymbol{\sigma}_{\mathrm{i}} \cdot \boldsymbol{\sigma}_{\mathrm{j}}. \tag{2.11}$$

Here J_{ij} is the exchange coupling constant between to spins $\mathbf{S}_i$ and $\mathbf{S}_j$. Positive J_{ij} corresponds to ferromagnetic coupling. This expression can be written in another form by using Dirac's spin exchange operator $\mathbf{P}_{\mathrm{ij}}^{\mathrm{spinex}}$, that exchanges the spin on electron j with the spin on electron i, as [44]:

$$\boldsymbol{\sigma_i} \cdot \boldsymbol{\sigma_j} = 2(\mathbf{P}_{\mathrm{ij}}^{\mathrm{spinex}} - \frac{1}{2}). \tag{2.12}$$

In a spin wave system the ground state represents a state where all spins are aligned in the same direction; spin up. A state with one magnon, one spin excitation may be represented by a superposition of orthogonal base states:

$$|\phi\rangle = \sum_n C_n \, |n\rangle \, e^{-iEt/\hbar} \tag{2.13}$$

where the time independent state $|n\rangle$ is defined as a state in which electron n has spin in the opposite direction; spin down. C_n is the amplitude that the opposite spin is on the n'th electron. As discussed in Section 2.1, the exchange interaction requires an overlap of wavefunctions and is therefore greatest for nearest neighboring electrons. In the first approximation, where only the nearest neighbor interactions are considered, the spin exchange operator has the following features:

$$\mathbf{P}_{3,4} \, |\mathrm{n}_3\rangle = |\mathrm{n}_4\rangle \tag{2.14}$$

$$\mathbf{P}_{2,3}\left|\mathrm{n}_3\right\rangle = \left|\mathrm{n}_2\right\rangle \tag{2.15}$$

$$\mathbf{P}_{4,5}\left|\mathrm{n}_3\right\rangle = \left|\mathrm{n}_3\right\rangle . \tag{2.16}$$

To simplify the calculations that follows, the ground state energy may be set to zero. Then the spin exchange operator is given by:

$$\boldsymbol{\sigma_i} \cdot \boldsymbol{\sigma_j} = 2(\mathbf{P}_{\mathrm{ij}}^{\mathrm{spinex}} - 1) \tag{2.17}$$

and the Hamiltonian is:

$$\mathcal{H} = -J_{ij} \sum_{\mathrm{ij}} (\mathbf{P}_{\mathrm{ij}} - 1), \tag{2.18}$$

with J being a term representing the nearest neighbor interaction between the spins. When acting on a base state $|n\rangle$, each pair of nearest neighbor adds a set of terms:

$$\mathcal{H}\left|n\right\rangle = -2J\Big(\left|n_{i+1}\right\rangle + \left|n_{i-1}\right\rangle - 2\left|n_i\right\rangle \Big). \tag{2.19}$$

Equation (2.19) is the Hamiltonian acting on the base state $|n\rangle$ in a system where electron n has two nearest neighbors. The base states may be assumed to be plane waves in the form:

$$\left|n\right\rangle = A_n e^{i\vec{k}\cdot\vec{r}_n} \tag{2.20}$$

where A_n is the amplitude of the spin wave at electron n and $\vec{r}_n$ is the position of electron n. The spin waves studied in this thesis are surface spin waves, with k-vectors pointing in one specific direction. The amplitude A_n may be assumed to be the same for electrons belonging to the same surface layer. The base states may therefore be written as:

$$\left|n\right\rangle = A_i e^{i\vec{Q}_\parallel\cdot\vec{r}_n} \tag{2.21}$$

where $Q_\parallel$ is the magnon wave vector direction in the surface plane and A_i is the amplitude of a spin wave in surface layer i. When the Hamiltonian operator acts on such a base state, $|n\rangle$, with two nearest neighbors, placed at positions $\pm\vec{r}_j$ from $\vec{r}_n$, the result is:

$$\mathcal{H}A_1 e^{i\vec{Q}_\parallel\cdot(\vec{r}_n)} = -2J_\parallel\Big[A_1\big(e^{i\vec{Q}_\parallel\cdot(\vec{r}_n+\vec{r}_j)} + e^{i\vec{Q}_\parallel\cdot(\vec{r}_n-\vec{r}_j)} - 2e^{i\vec{Q}_\parallel\cdot\vec{r}_n}\big)\Big] \tag{2.22}$$

$$\Rightarrow \mathcal{H}A_1 = -2J_{\parallel}\Big[A_1\big(2\cos\left(\vec{Q}_{\parallel}\cdot\vec{r}_j\right)-2\big)\Big]. \tag{2.23}$$

Here $J_{\parallel}$ is the exchange constant for exchange in the same plane. In case of a base state $|n\rangle$ that, in addition to the two in-plane nearest neighbors, also have nearest neighbors in a neighboring layer, placed at positions $\pm\vec{r}_l$ from $\vec{r}_n$, the result becomes:

$$\begin{aligned}\mathcal{H}A_1 e^{i\vec{Q}_{\parallel}\cdot(\vec{r}_i)} = \quad & -2J_{\parallel}\Big[A_1\big(e^{i\vec{Q}_{\parallel}\cdot(\vec{r}_i+\vec{r}_j)}+e^{i\vec{Q}_{\parallel}\cdot(\vec{r}_i-\vec{r}_j)}-2e^{i\vec{Q}_{\parallel}\cdot\vec{r}_i}\big)\Big] \\ & -2J_{\perp}\Big[A_2\big(e^{i\vec{Q}_{\parallel}\cdot(\vec{r}_i+\vec{r}_l)}+e^{i\vec{Q}_{\parallel}\cdot(\vec{r}_i-\vec{r}_l)}\big)-A_1\big(2e^{i\vec{Q}_{\parallel}\cdot\vec{r}_i}\big)\Big]\end{aligned} \tag{2.24}$$

$$\Rightarrow \mathcal{H}A_1 = -\Big[4J_{\parallel}\big(\cos\left(\vec{Q}_{\parallel}\cdot\vec{r}_j\right)-1\big)-4J_{\perp}\Big]A_1-\Big[4J_{\perp}\cos\left(\vec{Q}_{\parallel}\cdot\vec{r}_l\right)\Big]A_2. \tag{2.25}$$

Here $J_{\perp}$ is the exchange constant for interlayer exchange with the neighboring layer. The last term in Eq.(2.25) describes the situation in which a magnon from layer 1 exchanges to layer 2. The system studied in this thesis is assumed to consist of large patches with 2 ML. The Hamiltonian then has the form:

$$\mathcal{H}\,|n,m\rangle = \begin{bmatrix}\left[2J_{\parallel}\left(N_1^{\parallel}-\Sigma e^{i\vec{Q}_{\parallel}\cdot\vec{r}_j}\right)+2J_{\perp}N_1^{\perp}\right]e^{i\vec{Q}_{\parallel}\cdot\vec{r}_n} & \left[-J_{\perp}\Sigma e^{i\vec{Q}_{\parallel}\cdot\vec{r}_l}\right]e^{i\vec{Q}_{\parallel}\cdot\vec{r}_n} \\ \left[-J_{\perp}\Sigma e^{i\vec{Q}_{\parallel}\cdot\vec{r}_l}\right]e^{i\vec{Q}_{\parallel}\cdot\vec{r}_m} & \left[2J_{\parallel}\left(N_2^{\parallel}-\Sigma e^{i\vec{Q}_{\parallel}\cdot\vec{r}_j}\right)+2J_{\perp}N_2^{\perp}\right]e^{i\vec{Q}_{\parallel}\cdot\vec{r}_m}\end{bmatrix}\cdot\begin{bmatrix}A_1\\A_2\end{bmatrix} \tag{2.26}$$

where the state:

$$|n,m\rangle = \begin{bmatrix}A_1 e^{i\vec{Q}_{\parallel}\cdot\vec{r}_n}\\A_2 e^{i\vec{Q}_{\parallel}\cdot\vec{r}_m}\end{bmatrix} \tag{2.27}$$

is the base state and represents one magnon per layer. The Hamiltonian allows for magnons to move between the layers. $\mathrm{N_i^{\parallel}}$ is the number of nearest neighbors in layer i and $\mathrm{N_i^{\perp}}$ is the number of nearest neighbors in the neighboring layer from layer i. The vectors $\pm\vec{r}_j$ represent the neighbor position from $\vec{r}_n$ in the same layer, and vectors $\pm\vec{r}_j$ the positions of neighbors in the neighbouring layer. Equation (2.26) can be shortened to:

$$\mathcal{H}\begin{bmatrix}A_1\\A_2\end{bmatrix} = \begin{bmatrix}2J_{\parallel}\left[N_1^{\parallel}-\Sigma\cos\left(\vec{Q}_{\parallel}\cdot\vec{r_j}\right)\right]+2J_{\perp}N_1^{\perp} & -2J_{\perp}\Sigma\cos\left(\vec{Q}_{\parallel}\cdot\vec{r}_l\right)\\ -2J_{\perp}\Sigma\cos\left(\vec{Q}_{\parallel}\cdot\vec{r}_l\right) & 2J_{\parallel}\left[N_2^{\parallel}-\Sigma\cos\left(\vec{Q}_{\parallel}\cdot\vec{r_j}\right)\right]+2\mathrm{J}_{\perp}N_2^{\perp}\end{bmatrix}\cdot\begin{bmatrix}A_1\\A_2\end{bmatrix} \tag{2.28}$$

in accordance to the shortening of Eq.(2.22) to Eq.(2.23), by dividing with $e^{i\vec{\mathrm{Q}}_{\parallel}\cdot\vec{\mathrm{r}}_{\mathrm{n}}}$. The sums are over nearest neighbors. The nearest neighbors in a layer of an two-layered fcc(111) surface are illustrated in Fig.2.5(a). The yellow points mark nearest neighbors in the same plane, while the red spots mark nearest neighbors in the plane below. The orange arrow mark the $\vec{\mathrm{Q}}_{\parallel}$-direction that has been measured in this thesis - the $\bar{\Gamma}$-$\bar{K}$ direction of the surface. The yellow arrows mark $r_{jQ\parallel}$, the projection of $\vec{r}_j$ onto $\vec{\mathrm{Q}}_{\parallel}$. The red arrows mark $r_{lQ\parallel}$, the projection of $\vec{r}_l$ onto $\vec{\mathrm{Q}}_{\parallel}$. There are 6 nearest

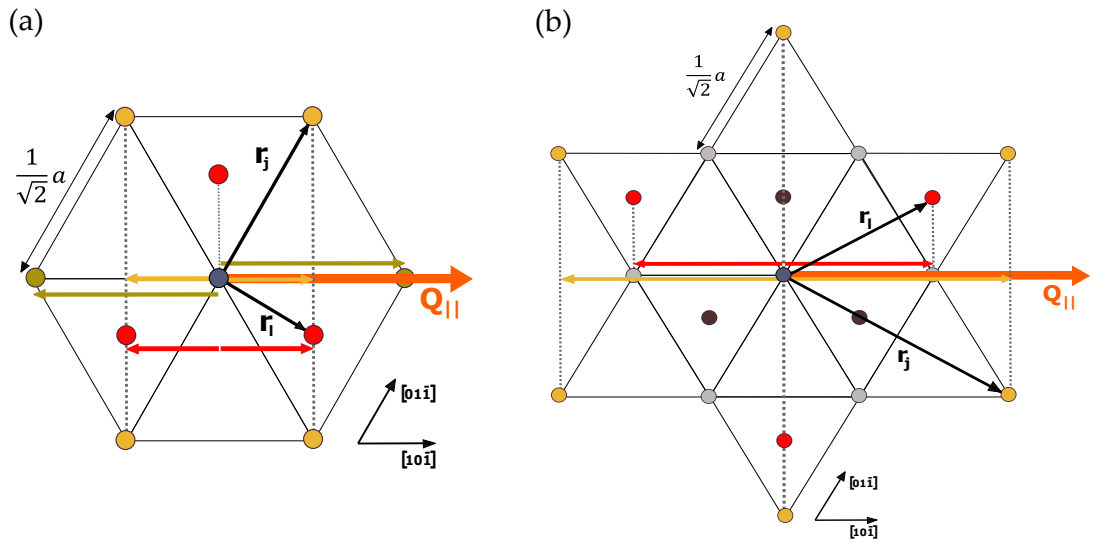

FIGURE 2.5: The **(a)** nearest and **(b)** next nearest neighbors on a fcc (111) surface. The yellow spots mark neighbors in the same layer, while the red spots mark neighbors in the layer below. A layer above would align itself like the red spots, but rotated 60° about the centre. See Fig. 2.4 for further clearance. The direction of momentum transfer $\vec{Q}_{\parallel}$, is marked by the orange arrow. The yellow arrows mark the projection of $\vec{r}_j$ onto the $\vec{Q}_{\parallel}$-direction. The red arrows mark the projection of $\vec{r}_l$ onto the $\vec{Q}_{\parallel}$-direction.

neighbors in the same plane, and three nearest neighbors in the plane below/above. Therefore both Layer 1 and Layer 2 have $N_1{}^{\parallel} = N_2{}^{\parallel} = 6$ and $N_1{}^{\perp} = N_2{}^{\perp} = 3$. Equation (2.28), the shortened version of the Hamiltonian acting on the base state Eq.(2.27), is given by Eq.(2.29).

$$\mathcal{H}\begin{bmatrix}A_1\\A_2\end{bmatrix} = \begin{bmatrix}2J_{\parallel}\left[6-2\cos\left(Q_{\parallel}\frac{a}{\sqrt{2}}\right)-4\cos\left(Q_{\parallel}\frac{a}{2\sqrt{2}}\right)\right]+6J_{\perp} & 2J_{\perp}\left[-1-2\cos\left(Q_{\parallel}\frac{a}{2\sqrt{2}}\right)\right]\\ 2J_{\perp}\left[-1-2\cos\left(Q_{\parallel}\frac{a}{2\sqrt{2}}\right)\right] & 2J_{\parallel}\left[6-2\cos\left(Q_{\parallel}\frac{a}{\sqrt{2}}\right)-4\cos\left(Q_{\parallel}\frac{a}{2\sqrt{2}}\right)\right]+6J_{\perp}\end{bmatrix}\begin{bmatrix}A_1\\A_2\end{bmatrix} \tag{2.29}$$

To get neater expressions, the Hamiltonian matrix entries in Eq.(2.29) may be written as variables a and b:

$$\begin{aligned} a &= 2J_{\parallel}\left[6-2\cos\left(Q_{\parallel}\frac{a}{\sqrt{2}}\right)-4\cos\left(Q_{\parallel}\frac{a}{2\sqrt{2}}\right)\right]+6J_{\perp},\\ b &= 2J_{\perp}\left[-1-2\cos\left(Q_{\parallel}\frac{a}{2\sqrt{2}}\right)\right]. \end{aligned} \tag{2.30}$$

The energy of the system is given by the time independent Schrödinger equation:

$$\mathcal{H}\left|\phi\right\rangle = E\left|\phi\right\rangle. \tag{2.31}$$

The right hand side in Eq.(2.31) is given by Eq.(2.26). The expression can be shortened by dividing both sides with $e^{i\vec{Q}_{\parallel}\cdot\vec{r}_n}$. Then the right hand side of Equation 2.31 is given by Eq.(2.29) and the resulting expression is:

$$\mathcal{H}\begin{bmatrix}A_1\\A_2\end{bmatrix} = \begin{bmatrix}a & b\\b & a\end{bmatrix}\begin{bmatrix}A_1\\A_2\end{bmatrix} = E\begin{bmatrix}A_1\\A_2\end{bmatrix}. \tag{2.32}$$

This eigenvalue-problem has non-trivial solutions if and only if:

$$\det\begin{bmatrix}a-E & b\\b & a-E\end{bmatrix} = 0. \tag{2.33}$$

The two non-trivial solutions for E are:

$$E_1 = a+b \quad \wedge \quad E_2 = a-b. \tag{2.34}$$

The resulting dispersion curves are illustrated in Fig. 2.6(a), by the dashed lines. The exchange coupling constants $J_{\parallel}$ and $J_{\perp}$ depends on the distances $\vec{r}_j$ and $\vec{r}_l$. As discussed in Section 2.3.1, is the inter-planar distance between the Co-layers less than that between layers of the substrate, $d_{Ir} = a_{Ir}/\sqrt{3}$. As seen in Fig. 2.5(a), the distance to the nearest neighbor in the same plane is:

$$d_j = \frac{1}{\sqrt{2}}a_{Ir} \approx 0.707 a_{Ir}, \tag{2.35}$$

while the distance to the nearest neighbor in a neighboring plane is:

$$d_l < \sqrt{\vec{r}_{\perp}^{\,2} + \vec{r}_{\parallel}^{\,2}} \approx 0.677 a_{Ir}. \tag{2.36}$$

From this it is clear that:

$$J_{\perp} > J_{\parallel}. \tag{2.37}$$

A better approximation may be achieved when including the next nearest neighbor in the calculation. Figure 2.5(b) illustrates the next nearest neighbors for a fcc (111) surface. The yellow spots indicate next nearest neighbors in the same plane, and the red ones the next nearest neighbors in the plane below. The next nearest neighbor interactions add:

$$\mathcal{H} = \begin{bmatrix}8J_{\mathrm{N}}^{\parallel}\big[1-\cos\left(Q_{\parallel}\frac{3a}{2\sqrt{2}}\right)\big] + 6J_{\mathrm{N}}^{\perp} & 2J_{\mathrm{N}}^{\perp}\big[-1-2\cos\left(Q_{\parallel}\frac{a}{\sqrt{2}}\right)\big]\\ 2J_{\mathrm{N}}^{\perp}\big[-1-2\cos\left(Q_{\parallel}\frac{a}{\sqrt{2}}\right)\big] & 8J_{\mathrm{N}}^{\parallel}\big[1-\cos\left(Q_{\parallel}\frac{3a}{2\sqrt{2}}\right)\big] + 6J_{\mathrm{N}}^{\perp}\end{bmatrix} \tag{2.38}$$

to the Hamiltonian in Eq.(2.29). Here $J_{\mathrm{N}}^{\parallel}$ is the exchange coupling constant for next nearest neighbors in the same layer, and $J_{\mathrm{N}}^{\perp}$ in neighboring layer. The solutions are

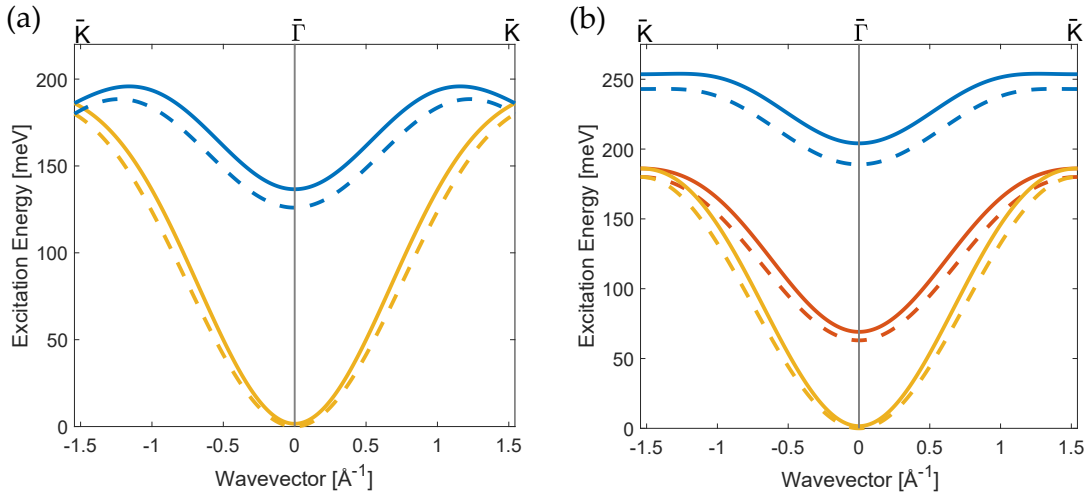

FIGURE 2.6: The calculated dispersion curves for magnons in a 2-layered (a) and 3-layered (b) fcc (111) structure. The solid lines are the calculated dispersion when only nearest neighbor interactions are considered. The dashed lines are the with next nearest neighbor interactions also included. In this simulation the exchange coupling constants are set at $J_{\parallel} = 6.5\,\text{meV}$, $J_{\perp} = 10.5\,\text{meV}$, $J_N^{\parallel} = 0.5\,\text{meV}$ and $J_N^{\perp} = 1.3\,\text{meV}$. The nearest neighbor is in the neighboring layer and therefore $J_{\perp} > J_{\parallel}$.

on the same form as given by Equations (2.34), with the variables a and b substituted by:

$$\begin{aligned} a' &= a + 8J_{\mathrm{N}}^{\parallel}\left[1 - \cos\left(Q_{\parallel}\frac{3a}{2\sqrt{2}}\right)\right] + 6J_{\mathrm{N}}^{\perp}, \\ b' &= b + 2J_{\mathrm{N}}^{\perp}\left[-1 - 2\cos\left(Q_{\parallel}\frac{a}{\sqrt{2}}\right)\right]. \end{aligned} \tag{2.39}$$

2.4.1 Trilayer structure

There could be patches of 3 layers in the system studied in this thesis as well. For a 3 layered structure the state:

$$|n,m,p\rangle = \begin{bmatrix} A_1 e^{i\vec{Q}_{\parallel}\cdot\vec{r}_n} \\ A_2 e^{i\vec{Q}_{\parallel}\cdot\vec{r}_m} \\ A_3 e^{i\vec{Q}_{\parallel}\cdot\vec{r}_p} \end{bmatrix} \tag{2.40}$$

is the base state with one magnon in each layer. The shortened Hamiltonian [Eq.(2.28)] has the form:

$$\mathcal{H}\begin{bmatrix} A_1 \\ A_2 \\ A_3 \end{bmatrix} = \begin{bmatrix} 2J_{\parallel}\left[N_1^{\parallel} - \Sigma e^{i\vec{Q}_{\parallel}\cdot\vec{r}_j}\right] + 2J_{\perp}N_1^{\perp} & -J_{\perp}\Sigma e^{i\vec{Q}_{\parallel}\cdot\vec{r}_l} & 0 \\ -J_{\perp}\Sigma e^{i\vec{Q}_{\parallel}\cdot\vec{r}_l} & 2J_{\parallel}\left[N_2^{\parallel} - \Sigma e^{i\vec{Q}_{\parallel}\cdot\vec{r}_j}\right] + 2J_{\perp}N_2^{\perp} & -J_{\perp}\Sigma e^{i\vec{Q}_{\parallel}\cdot\vec{r}_l} \\ 0 & -J_{\perp}\Sigma e^{i\vec{Q}_{\parallel}\cdot\vec{r}_l} & 2J_{\parallel}\left[N_3^{\parallel} - \Sigma e^{i\vec{Q}_{\parallel}\cdot\vec{r}_j}\right] + 2J_{\perp}N_3^{\perp} \end{bmatrix} \cdot \begin{bmatrix} A_1 \\ A_2 \\ A_3 \end{bmatrix} \tag{2.41}$$

Layer 1 and Layer 3 are identical to Layer 1 and Layer 2 of the 2-layer-calculation above, $N_1^{\parallel} = N_3^{\parallel} = 6$ and $N_1^{\perp} = N_3^{\perp} = 3$. The middle layer is a bit different since

a magnon there has probability of exchange both to the layer above and the layer below. The total number of nearest neighbors is therefore 12: $N_2^{\parallel} = 6$ and $N_2^{\perp} = 6$. Eq.(2.41) can be written on the form:

$$\mathcal{H} \begin{bmatrix} A_1 \\ A_2 \\ A_3 \end{bmatrix} = \begin{bmatrix} a & b & 0 \\ b & c & b \\ 0 & b & a \end{bmatrix} \begin{bmatrix} A_1 \\ A_2 \\ A_3 \end{bmatrix} \tag{2.42}$$

with the variables a and b defined by Eq.(2.30) and variable c defined by:

$$c = 2J_{\parallel}\big[6 - 2\cos(Q_{\parallel}\frac{a}{\sqrt{2}}) - 4\cos(Q_{\parallel}\frac{a}{2\sqrt{2}})\big] + 12J_{\perp}. \tag{2.43}$$

Again the time-independent Schrödinger equation of the system, Eq.(2.31), can be shortened by dividing both sides with $e^{i\vec{Q}_{\parallel}\cdot\vec{r}_n}$. Then the right hand side matches Eq.(2.42) and one can write:

$$\mathcal{H} \begin{bmatrix} A_1 \\ A_2 \\ A_3 \end{bmatrix} = \begin{bmatrix} a & b & 0 \\ b & c & b \\ 0 & b & a \end{bmatrix} \begin{bmatrix} A_1 \\ A_2 \\ A_3 \end{bmatrix} = E \begin{bmatrix} A_1 \\ A_2 \\ A_3 \end{bmatrix}. \tag{2.44}$$

This equation has the constraint:

$$\det \begin{bmatrix} a-E & b & 0 \\ b & c-E & b \\ 0 & b & a-E \end{bmatrix} = 0. \tag{2.45}$$

for non-trivial solutions. The three non-trivial solutions for E are:

$$E_1 = a \quad \wedge \quad E_{2,3} = \frac{a + c \pm \sqrt{(a+c)^2 - 4(ac - 2b^2)}}{2}. \tag{2.46}$$

The next nearest neighbor interactions adds:

$$\mathcal{H} = \begin{bmatrix} 8J_N^{\parallel}\big[1-\cos(Q_{\parallel}\frac{3a}{2\sqrt{2}})\big]+6J_N^{\perp} & 2J_N^{\perp}\big[-1-2\cos(Q_{\parallel}\frac{a}{\sqrt{2}})\big] & 0 \\ 2J_N^{\perp}\big[-1-2\cos(Q_{\parallel}\frac{a}{\sqrt{2}})\big] & 8J_N^{\parallel}\big[1-\cos(Q_{\parallel}\frac{3a}{2\sqrt{2}})\big]+12J_N^{\perp} & 2J_N^{\perp}\big[-1-2\cos(Q_{\parallel}\frac{a}{\sqrt{2}})\big] \\ 0 & 2J_N^{\perp}\big[-1-2\cos(Q_{\parallel}\frac{a}{\sqrt{2}})\big] & 8J_N^{\parallel}\big[1-\cos(Q_{\parallel}\frac{3a}{2\sqrt{2}})\big]+6J_N^{\perp} \end{bmatrix} \tag{2.47}$$

to the Hamiltonian in Eq.(2.42). The solutions are on the same form as given by Equations 2.46, with the variables a, b as substituted by a', b' defined in Eq.(2.39) and c substituted by:

$$c' = c + 8J_N^{\parallel}\big[1 - \cos(Q_{\parallel}\frac{3a}{2\sqrt{2}})\big] + 12J_N^{\perp}. \tag{2.48}$$

The three layer dispersion relation is shown by Fig. 2.6(b). Compared to the 2-layer dispersion in Fig. 2.6(a) the 3-layered dispersion has an extra mode, marked in red. Calculations of similar systems, based on a classical argument are represented in Refs.[17, 45].

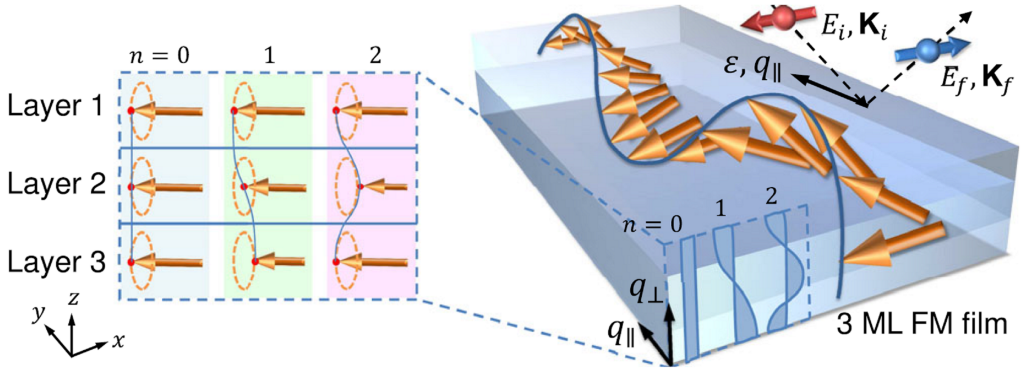

FIGURE 2.7: A schematic illustration of the energy modes in a 3 layered structure with identical boundary conditions of the top and bottom. The broken transnational symmetry in the the out-of-plane direction exerts a constraint on the out-of-plane wavevector $q_\perp$. The 3 allowed modes are standing spin waves and are represented by the left box. The quantum number n indicates how many nodes the mode has. The in-plane magnon wavevector is marked by $q_{||}$. E_i, K_i and E_f, K_f are the energy and wavevector of the incident and scattered electrons in a spin-polarized electron energy-loss spectroscopy (SPEELS) experiment. Figure taken from [19].

The different energy levels may be understood as a phase shift of the spin wave in each layer. The lowest energy band corresponds to a situation in which the spin wave of each layer are in phase. The higher energy bands corresponds to the spin waves of each layer being out of phase. In the out-of-plane direction the translation symmetry is broken, and this exerts a constraint on the magnons. The allowed magnon states in the out-of-plane direction are quantized standing spin waves with wave vector $q_\perp = n\pi/d$, where d is the film thickness and n is the quantum number. In a system with 3 layers there are three allowed out-of-plane magnon modes. A schematic representation of the three modes are shown in Fig. 2.7. The quantum number n represents the number of nodes inside the film. For $n = 0$ there are coherent precession between the layers and therefore zero nodes. The $n = 1$ and $n = 2$ modes has one and two nodes inside the film. It has been observed, in earlier measurements done at our lab, that higher energy magnon modes are more strongly damped and have shorter lifetime than the low energy modes. This has been attributed to the stronger damping that occurs as higher energy modes precess out of phase between the layers. Generally the higher energy magnons show stronger damping due to dissipation to the Stoner continuum. This effect comes on top of

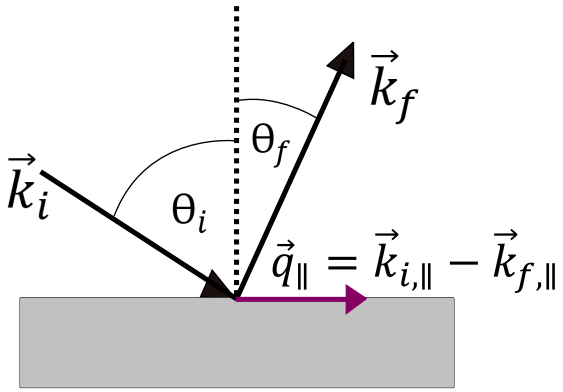

FIGURE 2.8: Due to transnational symmetry, the in-plane component of $\vec{k}$ is conserved during scattering experiments on a (smooth) surface. Here, $\vec{k}_i$, θ_i and $\vec{k}_f, \theta_f$ are the incident and final wavevectors and angles respectively. The transferred in-plane momentum $\vec{q}_\parallel = \vec{k}_i - \vec{k}_f$.

that. A magnon of mode $n = 1$ that has the same energy as a magnon of mode $n = 0$, is expected to have stronger damping than the magnon of mode $n = 0$.

2.5 Inelastic electron scattering

The work of this thesis is based on spin-polarized electron energy-loss spectroscopy (SPEELS) experiments, that is a type of inelastic electron scattering technique. Inelastic scattering is a scattering process in which the kinetic energy of the incident particle is not conserved. In a surface scattering experiment the transnational symmetry is conserved in the in-plane direction, but broken in the out-of-plane direction. According to Noether's theorem [46], the in-plane momentum is therefore conserved, which means that the in-plane wavevector $\vec{k}$ is also conserved through a scattering event. Thus:

$$\vec{k}_{i,\parallel} = \vec{k}_{f,\parallel} + \vec{q}_\parallel \tag{2.49}$$

with $\vec{\mathrm{k}}_{\mathrm{i},\parallel}$ and $\vec{\mathrm{k}}_{\mathrm{f},\parallel}$ being the incident and final wavevector in the plane-parallel direction and $\vec{\mathrm{q}}_\parallel$ being the plane-parallel momentum transfer. The energy lost in the scattering process is:

$$E_{loss} = E^i_{kin} - E^f_{kin} \tag{2.50}$$

A general surface-scattering event is schematically illustrated in Fig. 2.8. Inelastic electron scattering may be divided into two regimes; dipole scattering and impact scattering. In dipole scattering the incoming electron scatters off the electric dipolar field that may be created by the charge carriers on the surface, in particular surface plasmons. The electrons scatter here, for the most part before they reach the surface. The energy loss is small and therefore dipole scattering is typically strongest observed

close to the specular beam in scattering experiments. In impact scattering the incoming electron penetrates the surface and scatters by impact. In contrast to the dipole scattering regime, the incoming electron may here get at such a low distance to the electrons in the sample, that exchange processes are possible. The possible outcomes of inelastic scattering of a electron beam consisting of minority electrons, is shown in Fig. 2.9. The yellow arrows represent the incoming (minority) electrons having an energy E_{kin} before the scattering event. The blue arrows represent the electrons of the sample, that can both be of minority and majority spin. E_F is the Fermi energy and E_{loss} is the energy lost in the scattering process. The energy loss of the electron leads to an excitation of the electron in the sample. From the left, the first possibilities are that the incoming electron of minority spin loose energy E_{loss} and transfer it to an electron in the sample that is either of majority of minority spin. The incoming electron of minority spin may also exchange with an electron in the sample that are either of minority or majority character. The only spin flip process is illustrated to the right, where the incoming minority electron exchanges with a majority electron of the sample. This exchange process leads to a magnon excitation in the sample. The magnon excitation can be distinguished from other excitations by comparing the signal from scans with the incoming beam being of minority and majority character. A magnon peak will show when the incoming electrons are of minority spin. The peak will vanish for an incoming beam of electrons of majority spin. Other excitations that may contribute to the low energy inelastic scattering intensity spectra are phonons, excitons, vibrational modes of adsorbates, and excitation of conduction band electrons.

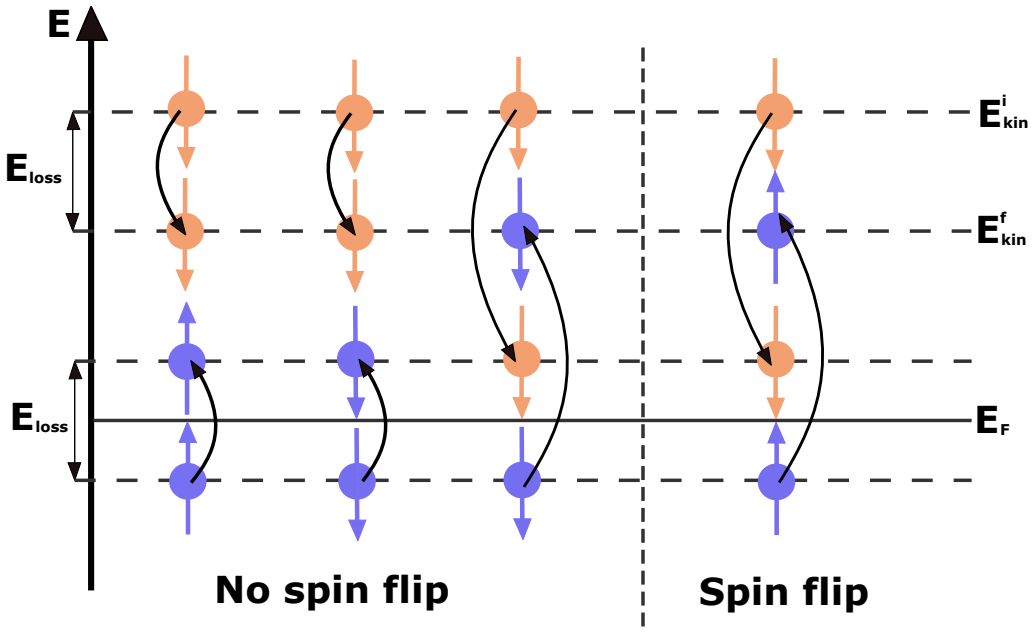

FIGURE 2.9: Four possible outcomes of inelastic electron scattering with incoming electrons (yellow arrows) being of minority spin. The blue arrows represents the electrons of the sample. The incoming electron may loose energy E_{loss} and transfer it to an electron in the sample, that can be of either minority or majority spin. This would lead to no total spin flip in the sample, and is illustrated by the two cases furthermost to the left. The exchange processes are illustrated by the two cases furthermost to the right. If an incoming minority electron exchanges with an minority electron of the sample there is again no total spin flip in the sample. The magnon excitation occurs when a incoming electron of minority spin exchanges with an electron of the sample with majority spin. Figure inspired by [40]

Chapter 3

Experimental Setup

3.1 Overview

The experiments are performed in an ultrahigh vacuum (UHV) system (section 3.1.1) consisting of three chambers, as illustrated in Fig. 3.1. In the **Preparation chamber** (Section 3.3), a GaAs photocathode is cleaned and prepared by adsorption of Cs and Cs_2O. This photocathode is later used as the source of the spin-polarized electron beam in the SPEELS-experiment. In the **Analysis Chamber** (Section 3.2) the sample is cleaned and prepared. An epitaxial film of Co is grown on an Ir(111) substrate by means of an electron beam evaporator. Additionally, the chamber is used for MOKE-, AES- and LEED-measurements. The SPEELS-experiment is performed in the **SPEELS chamber**(Section 3.4). There, the photo-emitted electron

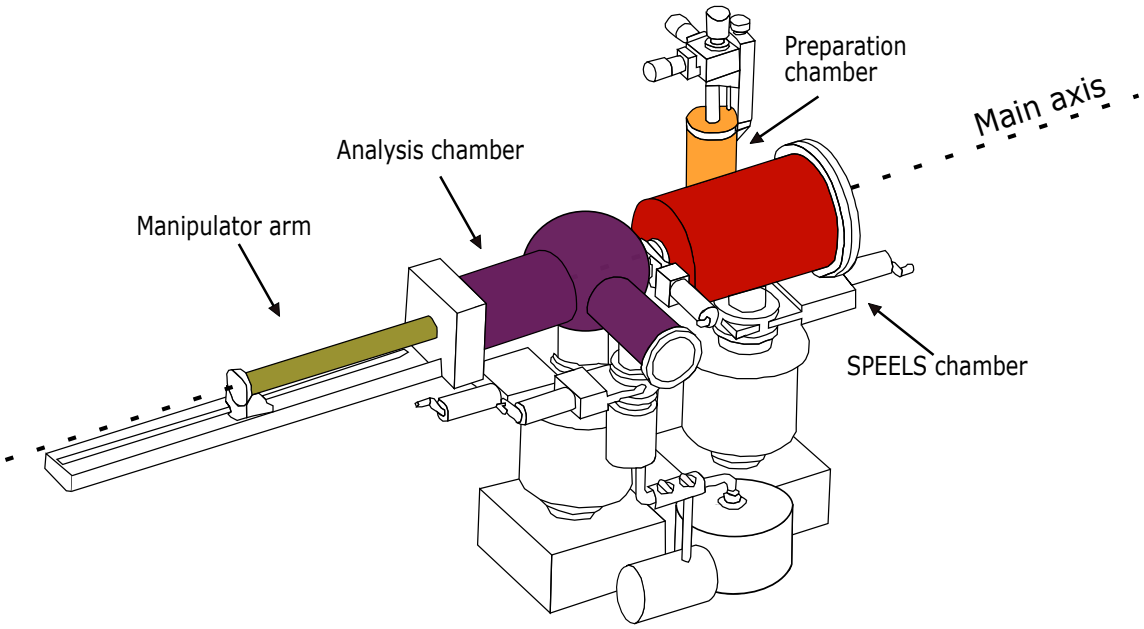

FIGURE 3.1: The UHV system. The sample is located at the end of the manipulator arm and can be moved from the Analysis chamber to the SPEELS-chamber. The GaAs photocathode is prepared in the Preperation chamber and moved via a wobble stick to the SPEELS chamber. Graphic inspired from [45]

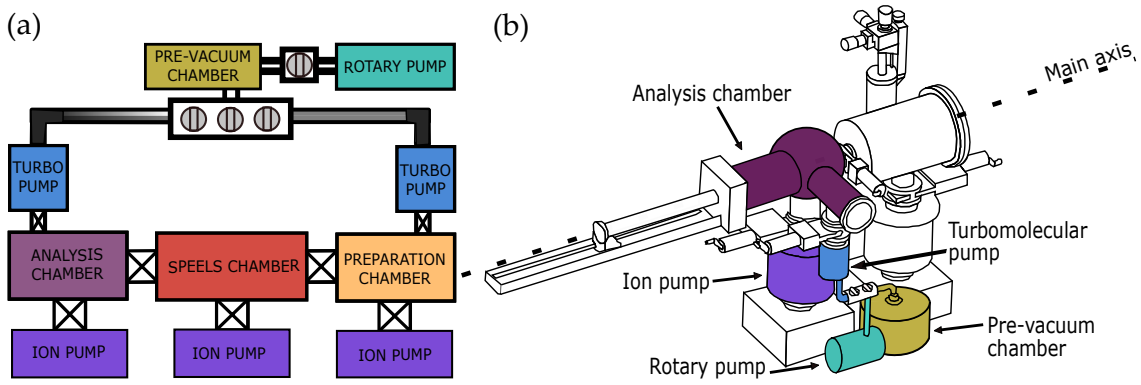

FIGURE 3.2: **(a)** A schematic illustration of the UHV system. All chambers have an ion pump connected to them, while only the preparation chamber and the analysis chamber are each connected to one turbomulecular pump. The crossed areas in between the chambers represent UHV isolation valves. **(b)** The UHV system with colors marking the components used for pumping the Analysis chamber.

beam is accelerated, focused and energetically dispersed as it goes through a 90° and 180° monochromator, before it hits the sample. The scattered electrons pass through an analyzer before they are collected by a channeltron. The energy of the electrons is measured by the analyzer. The momentum transfer from the electron beam onto the sample can be altered by a sample rotation which is changing the scattering geometry.

3.1.1 Ultrahigh Vacuum

All investigations and preparations for SPEELS are surface sensitive and require to be performed in UHV environment. This UHV environment is substantial, to reduce surface contamination to a minimum, but also to ensure a sufficiently long free path of the electron beam in the electron scattering experiment. The chambers can reach pressures down to 2×10^{-11} mbar and are well within the 10^{-11} mbar-range during measurements. To be able to obtain such good pressures a sophisticated pump system as well as securely sealed vacuum-chambers are necessary. The chambers are made of stainless steel and are sealed by copper gaskets. A schematic representation of the pump system is given in Fig. 3.2(a). In Fig. 3.2(b) the pump setup of the Analysis Chamber is sketched. Starting from atmospheric pressure, the first activated pump is the rotary pump. It pumps the pre-vacuum chamber down to 8×10^{-2} mbar and is automatically reactivated when the pressure reaches 2×10^{-1} mbar. The turbomolecular pump is used for pumping the chamber pressure down to the 10^{-8} mbar-range.The turbomolecular pump exhausts to the pre-vacuum chamber. Finally, the ion pump is used from the 10^{-8} mbar-range on. All the chambers are also equipped with a titanium sublimation pump as a supplement to the ion

pump. In addition to the pumps, the bottom part of the chamber walls are continuously cooled by liquid nitrogen. In theory, pressures down to the 10^{-12} mbar-range can be achieved, but this would require stronger cooling. The chamber-pressure is measured with a hot-filament ionization gauge.

3.2 Analysis Chamber

3.2.1 Growth of Co films

The Co film is grown using an electron beam evaporator, as illustrated in Fig. 3.3. High voltage ($U_{max} = 866\,\mathrm{V}$) is applied to the Co rod positioned in the middle of the cylindrical chamber. A filament loop surrounds the tip of the rod and once a current flows ($I_{filament} \approx 2.02\,\mathrm{A}$) some of the electrons will detach from the filament, accelerate towards, and hit the rod. This causes an emission current bombarding the rod of about $I_{emission} \approx 11.2\,\mathrm{mA}$. The electron bombardment causes intense local heating of the tip of the rod, as well as scattering of some clusters of Co atoms and ions. When the shutter is opened, the gas flows into the Analysis Chamber and can be adsorbed onto the substrate. The flux of clusters leaving the evaporator is

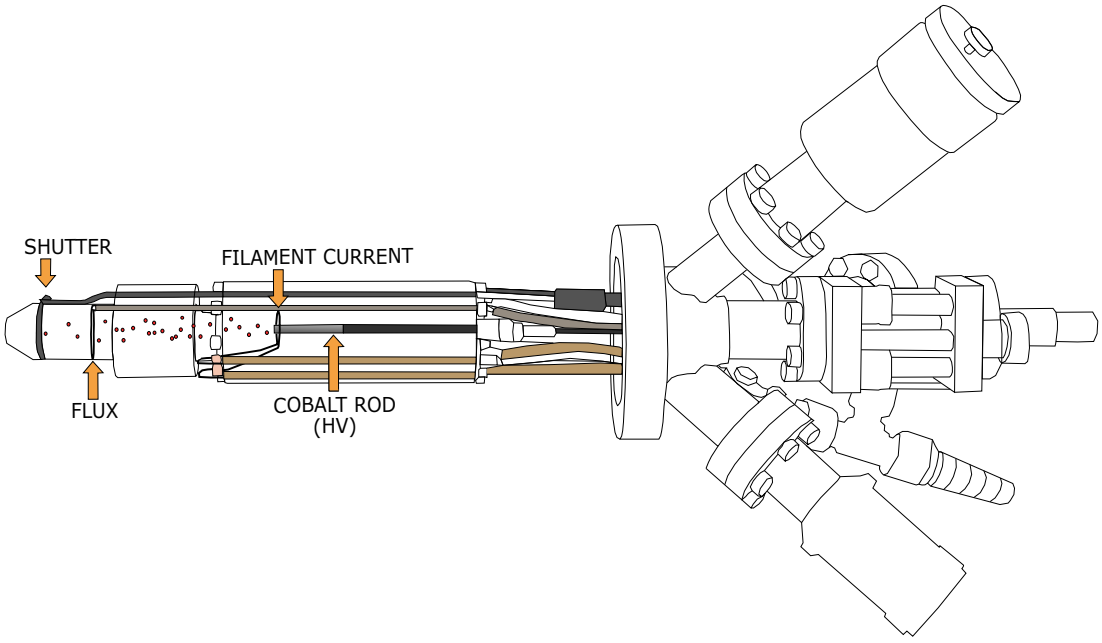

FIGURE 3.3: Sketch of the electron beam evaporator used to deposit Co. The Co rod inside the cylinder is at high voltage (HV), so that electrons from the filament current will accelerate towards it. This electron bombardment causes intense local heating at the tip of the rod, as well as scattering of some clusters of Co atoms and ions. When the shutter is open the gas can flow out and will be adsorbed onto the substrate. Some ions will attract to the flux loop creating a current. This current is directly proportional to the amount of Co deposited.

measured using a flux monitor. Some ions will attract to the flux loop and cause a current ($I_{flux} \approx 60\,\text{nA}$) that is directly proportional to the gaseous flow towards the shutter. This current can therefore be used to determine the amount of Co deposited at the substrate. After calibration (Section 3.5), it was found that a monolayer of Co corresponds to the deposition of 10 µC. For this thesis 1.6 ML of Co was grown, with the deposition of 15.9 µC.

3.2.2 Flashing and Annealing

Flashing and annealing are both about heating the sample by electron bombardment. Annealing is used to make the Co surface smoother, while flashing is used to remove the film and residual gases from the substrate. Before a new sample is grown, the old sample and residual gases must be removed from the substrate by flashing. The samples investigated in this thesis were flashed twice for 20 s with a filament current of $I_{filament} = 3.4\,\text{A}$, a HV of 620 V and a resulting emission current of $I_{emission} = 150\,\text{mA}$. The Co films were deposited after the substrate was cooled down to room temperature. A new Co film can be made smoother by annealing. Research have also revealed that the easy axis of the magnetization of Co grown on Ir(111) is stabilized after annealing treatments [47]. It is however important that the temperature obtained during each annealing treatment does not overcome 600 °C. Annealing at higher temperatures than this results in alloy formations and Ir segregation on the surface [48]. In this work, the films were annealed $2-3$ times for 99 s with $I_{filament} = 2.4\text{A}$, a HV of 800 V and a resulting emission current of $I_{emission} = 2\,\text{mA}$. With this approach the temperature of the sample was kept safely beneath the critical temperature for alloy formations. In between the annealing steps, the sample was left for thermalization with its environment for half an hour.

3.2.3 MOKE

Magneto Optic Kerr Effect (MOKE) measurements [49], were used to test the magnetic properties of the sample, and to calibrate the film thickness as a function of deposited Co. MOKE measurements were performed in the longitudinal geometry [50]. Fig. 3.4 shows an illustration of the setup. The magnetic field produced by the electromagnets are in the in-plane direction of the sample. Incident polarized laser light ($\lambda = 650\,\text{nm}$) is reflected from the surface and the Kerr rotation of the reflected beam is measured by the analyzer and detector. The analyzer consists of two polarizers set at almost 90° against one another. The offset of 90° ensures that there is a signal transmitted to the detector while the intensity is very sensitive to

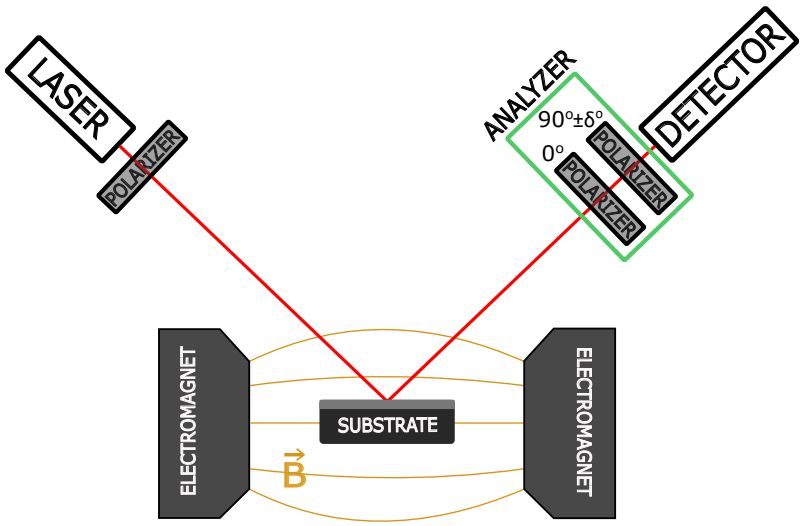

FIGURE 3.4: Illustration of the MOKE setup. The substrate with a thin Co film on it is placed in an in-plane magnetic field produced by electromagnets. Incident polarized laser light is reflected from the surface and the polarization of the reflected beam is measured by the analyzer and detector.

rotations in the incoming polarization. The light intensity that passes through a polarizer is proportional to $\cos^2(\theta)$ [51]. The derivative of this is higher for angles deviating from 90° and therefore such angles are preferable.

3.2.4 Auger Electron Spectroscopy

After flashing it is necessary to check whether the substrate is clean. This is done by running an Auger scan over the substrate [52, 53]. The Auger spectrometer consists of a cylindrical mirror analyzer (CMA) integrated with a coaxial electron gun. Fig. 3.5 shows a sketch of the spectrometer. An electron beam of 3 kV is focused onto the substrate and expels some core electrons as it penetrates the surface, creating a hole. Now, a higher energy electron can recombine with the hole, releasing its energy either by emitting an X-ray photon, or by transmitting its energy to another high level electron that is then ejected from the atom. The latter process is termed Auger recombination and the ejected electrons are called Auger electrons. For atoms near the surface, these Auger electrons have a high chance to be emitted from the film. The emitted electrons are deflected around the electron gun and pass through an aperture before reaching the cylindrical mirror analyzer. After passing a second aperture the electrons are collected by the channeltron. The energy of the electrons that can pass through the aperture to the channeltron is determined by the voltage in the cylindrical mirror analyzer. In this way, the energy spectra of the emitted electrons is measured and the spectra of the compounds present at the surface can be identified [54]. During an Auger scan CO and CO_2 molecules, caused by the electron

beam stimulated desorption, adsorb on the surface. It is therefore necessary, to flash the substrate after an Auger scan, before a new film can be grown on it.

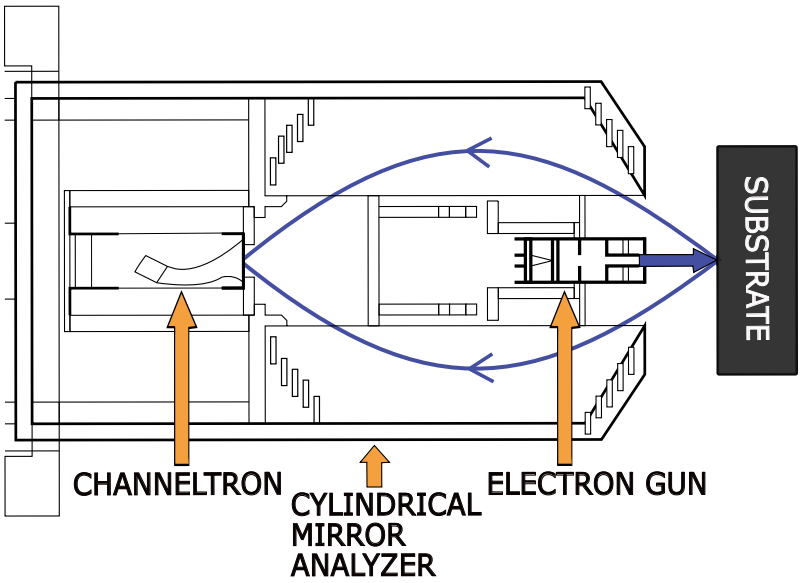

FIGURE 3.5: Sketch of the Auger spectrometer. An electron beam is focused onto the substrate and the emitted Auger electrons are passing through the cylindrical mirror analyzer before they reach the channeltron where they are measured.

3.2.5 LEED

Low Energy Electron Diffraction (LEED) can be used to investigate the orientation of the surface of the substrate crystal. The LEED pattern shows the reciprocal lattice of the surface. The orientation of the reciprocal lattice tells what orientation the surface structure has. The LEED measurement is done by shooting a beam of low energy electrons on the substrate. Those electrons will penetrate the first few layers of the surface. Some will scatter and diffract back towards the electron gun. The diffraction pattern of the scattered electrons is recorded on a fluorescent screen wrapped on a hemisphere-surface behind the electron gun. To filter out the inelastically scattered electrons electric grids are placed on the way from the substrate to the fluorescent screen.

3.3 Preparation Chamber

3.3.1 Photocathode Preparation

In 1976 D. T. Pierce and F. Meier showed that GaAs can be used to create a spin-polarized electron beam [55]. Due to spin-orbit interaction, the $P_{1/2}$ and $P_{3/2}$ valence bands of GaAs lie at different energy levels. The bands are illustrated in

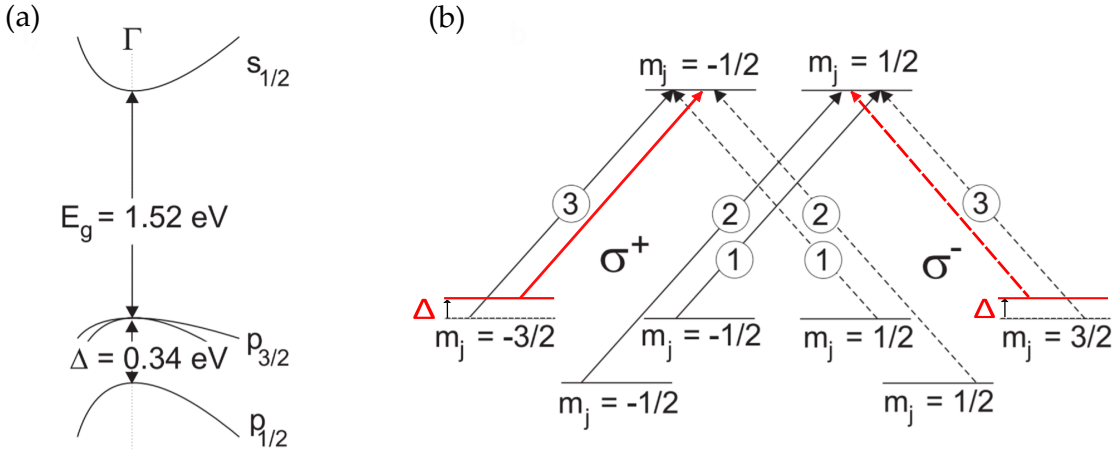

FIGURE 3.6: **(a)** A schematic representation of the valence and conduction bands of GaAs. **(b)** A schematic illustration of the energy levels of GaAs. The transitions that require a spin-flip of $\Delta S = 1$, are marked by σ^+. The transitions that require a spin-flip of $\Delta S = -1$, are marked by σ^-. The red lines illustrates the lift of the $m_j =\mid 2/3 \mid$ states, that can be obtained by adding strain to the GaAs lattice at the surface. This increases the transition polarization. Graphic inspired from [40]

Fig. 3.6 (a). When illuminating the GaAs with light finely tuned to the energy $E_g = 1.52\,\text{eV}$, only transitions from the $P_{2/3}$ band are allowed. In Fig. 3.6(b) the energy levels are illustrated and marked to show the different transitions from the valence P-band to the S-conduction band. The transitions that require a spin-flip of $\Delta S = 1$, and are thus excited by right circular (RC) polarized light, are marked by σ^+. The transitions that require a spin-flip of $\Delta S = -1$, and thus are excited by left circularly (LC) polarized light, are marked by σ^-. Each transition is marked with numbers $1-3$. The transitions marked by 2 are the transitions from the $P_{1/2}$ band to the S band, that are not allowed for energies finely tuned to $E_g = 1.52\,\text{eV}$. Under such conditions the transitions 1 and 3, the ones from the $P_{3/2}$ band to the S band, are the ones contributing to the electrons in the conduction band. As can be seen in Fig. 3.6, both spin up and spin down electrons can be excited to the conduction band for both LC- and RC-polarization of the incoming light. To increase the transition polarization, it is possible to lift the energy of the $m_j =\mid 3/2 \mid$ states by adding strain to the GaAs lattice at the surface. This can be done by growing layers of $GaAs_{x-1}P_x$ epitaxially on the surface of the cathode[56], and is done by the manufacturer of the cathode. The transition from the lifted $P_{3/2}$ $m_j =\mid 3/2 \mid$ energy levels to the S band are marked in red. The energy of this transition is $E = E_g - \Delta \approx 1.49$ and corresponds to a wavelength of $\lambda \approx 830\,\text{nm}$ [57], which is the wavelength of the laser used during the experiment. As the incident light is finely tuned to $E = 1.49$, the main excitations contributing to the electrons in the conduction band are from the $m_j =\mid 3/2 \mid\rightarrow$ S-transitions. For RC polarization

the transition is from $m_j = -3/2 \rightarrow m_j = -1/2$ and for LC polarization the transition is from $m_j = 3/2 \rightarrow m_j = 1/2$. With this manufacturing method the conduction band can reach spin polarizations up to 90 % [40]. The purpose of the cathode is to create an electron beam, and therefore the workfunction must be as low as possible. For a clean GaAs-surface, however, the workfunction is too high to produce an significant electron beam. The workfunction can be reduced drastically by adsorption of layers of Cs and Cs_2O on the surface [55]. These layers are very sensitive to contaminations and must be freshly grown every week. Before new layers can be grown, the GaAs cathode must be cleaned. This is done by carefully heating it to about 570 K by resistive heating. After cooled down to about 370 K, the first layer of Cs is deposited. The photocurrent is measured during the deposition and after a peak in the photocurrent, O_2 is added to the chamber to create a layer of Cs_2O. As the photocurrent once again shows a peak, the O_2-valve is closed to grow the next layer of Cs. This cycle is repeated until 6 layers of Cs_2O are grown on top of the cathode. For each Cs layer, the O_2 is introduced when the photocurrent is about 1/2 of the peak value. For each Cs_2O layer, the O_2-valve is closed as the photocurrent is about 1/3 of the peak value. With this method, photocurrents up to 20 µA where reached. For the experiment, this current was reduced to about 10 µA by reducing the laser intensity with a polarizer, to ensure stability. The freshly prepared cathode can last up to 5 days, if it is held at good UHV-conditions.

3.4 SPEELS Chamber

3.4.1 SPEELS

In the SPEELS experiments a spin polarized electron beam scatters off the sample. The energy spectrum of the scattered electrons is measured, and the spectra rerecorded for each spin polarization of the incident electron beam. For films with in-plane magnetization, a magnon peak will show for the spin down direction, but not for the spin up direction. Phonons, vibrational modes and out-of-plane magnetic excitations will show equally well in both spectra. A schematic sketch of the experiment is shown in Fig. 3.7 and a Fig. 3.8 is a photo of the spectrometer. The spin polarized beam is generated by photoemission from the GaAs photocathode. The photoemission is initiated by a 830 nm laser, that, after going through a Pockels cell, is circularly polarized. The polarization switches between left- and right-circular polarization, as the voltage through the Pockels cell is varied. The polarization of the electron beam is determined by the polarization of the laser.

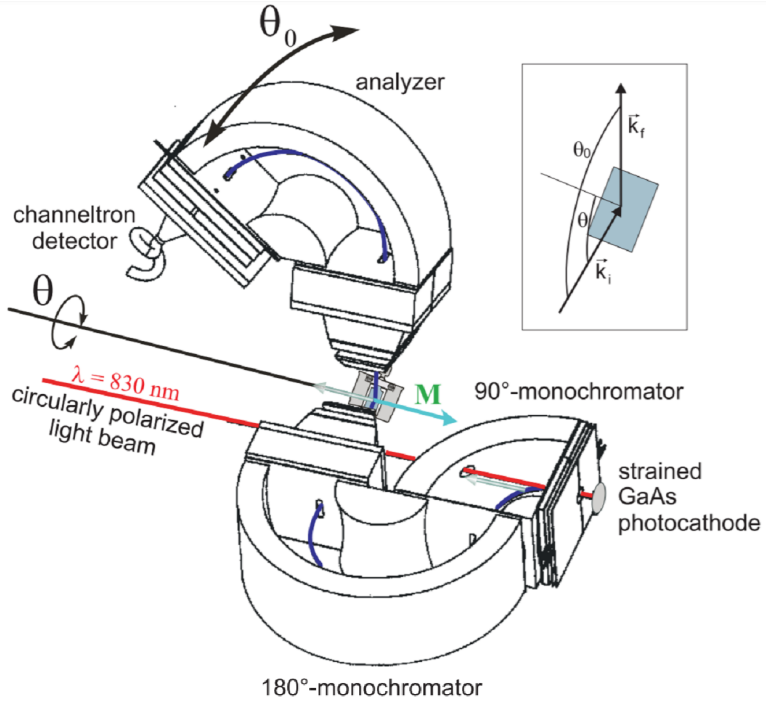

FIGURE 3.7: The spectrometer consisting of a 90° and 180° monochromator, an analyzer and a channeltron. The sample is positioned between the monochromator and the analyzer. The electron beam is generated by a 830 nm laser photoemitting the GaAs cathode. The monochromators and the analyzer are at a fixed angle $\theta_0 = 80°$ with respect to each other. In the upper right corner is sketch of the scattering geometry with the incident (k_i) and final (k_f) wavevector. Graphic taken from [40].

The spin polarized beam goes through a 90° and 180° monochromator, that energetically disperses, accelerate and focus the beam before it hits the sample. The angle of incidence is varied by rotating the manipulator arm, on which the sample is mounted. The scattered electrons are collected by the analyzer that only allow electrons with a specific energy, to pass through the aperture and be collected by the channeltron. Both, the monochromator and analyzer filter the electron energy by varying the voltage on the inner and outer curved plate and vary the size of the entrance and exit slits. An electron that travels through the device can only arrive at the exit slit if it has a specific energy. The resolution of the beam can be increased by reducing the size of the slit, but this is at the expense of lower beam intensity. The components can be seen in Fig. 3.8, where also the head of the manipulator arm is part of the photo. The monochromator and analyzer are fixed at an angle $\theta_0 = 80°$ with respect to each other. It is possible to change this angle by rotating the analyzer and detector using the rotatable arm, but this is never done in this thesis. The beam energies used in this work lie in the range of $3.2 - 4.5\,\text{eV}$. The resolution lies in the range of $14 - 19.6\,\text{meV}$. The SPEELS experiment is designed with ΔK being defined positive in the opposite direction as the momentum transfer

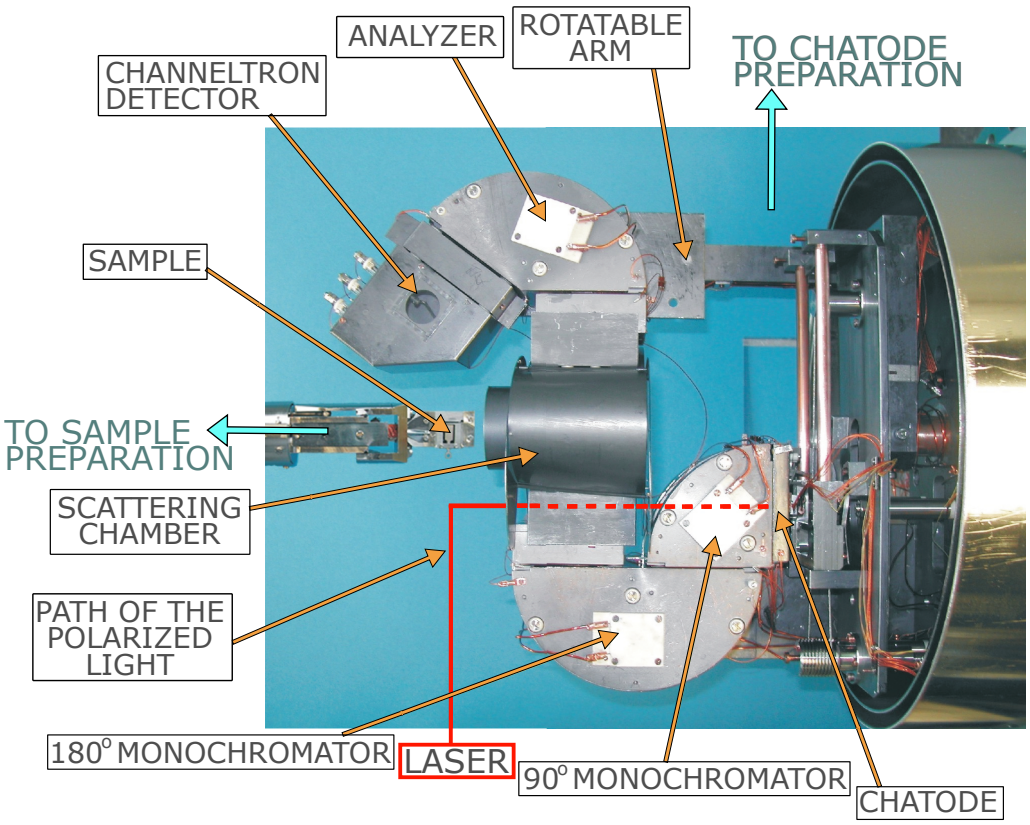

FIGURE 3.8: A photo of the spectrometer and the head of the manipulator. The different components are marked. The laser is reflected by a mirror that is not included in the picture. Graphic inspired from [40].

$\mathbf{q}$, in accordance with Equation 2.49. The scattering geometry is for positive ΔK like illustrated in Fig. 3.9(a), while for negative ΔK it is like illustrated in Fig. 3.9(b). For large magnitudes of ΔK, the incident angle θ_i goes towards 0° for the positive side, and towards 90° for the negative side. It is clear that the incident beam has a larger projection to the plane-parallel direction for negative ΔK. This may cause more general excitations in in-plane direction of the film, that are visible in the SPEELS spectra. The presence of more general excitations can make it harder to resolve the magnon peak. In addition, as $\theta_i \to 90°$ the incident beam may scatter off the sample holder and the corner of the sample, as well as the Co/Ir-surface at the other side of the corner (vertical orientation in figure). For positive ΔK, it is harder to excite in-plane excitations. As $\theta_i \to 0°$, the beam hits the sample at normal incidence and most of the electrons either penetrate the sample or are backscattered. However, with this geometry the measurements look clearer, and the magnon peaks are better resolved.

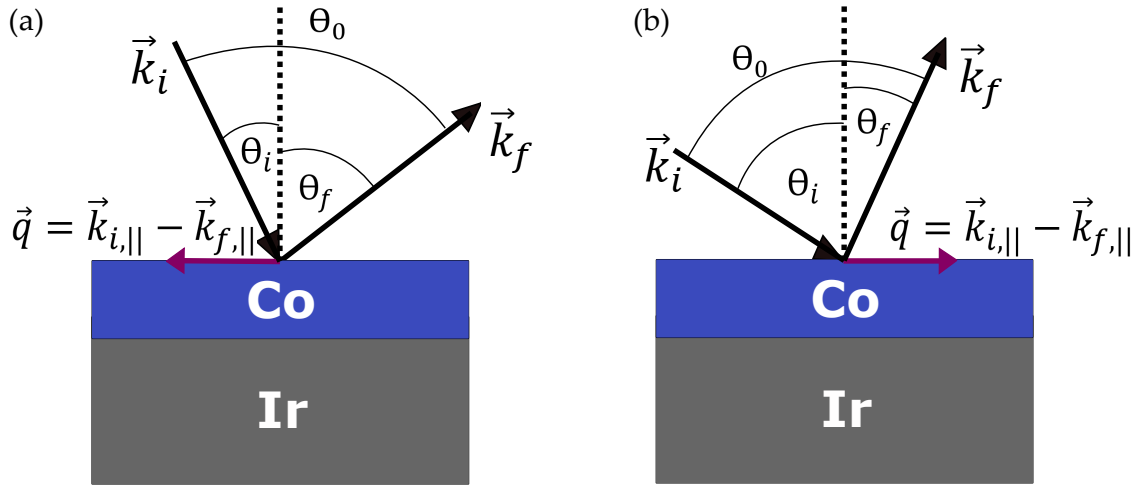

FIGURE 3.9: The scattering geometry for the positive (a) and negative (b) $\Delta\vec{K}$-direction.

3.5 Deposition Calibration

A calibration of the system is necessary to estimate how many atomic monolayers a certain amount of deposited Co is. The amount of monolayers deposited on a surface may be determined by RHEED (Reflection High Energy Electron Diffraction). For magnetic samples, the amount of Kerr rotation under MOKE is proportional to the number of atomic monolayers deposited. It is known, from earlier measurements on our lab, that for Co, deposited and measured at room temperature, on a W(110)-surface, the Kerr rotation develop as seen in Firgue 3.10(a). The point at which the linear curve crosses the y-axis, corresponds to 1ML of Co deposited [58]. A calibration that was done just before the measurements for this thesis begun, gave that 1ML correspond to 9 µC. There are no known measurements that relate the number of atomic monolayers to Kerr rotation for Co grown on an Ir(111)-surface. The amount of monolayers on the Ir(111) surface must therefore be estimated through calculation. The W(110) surface is illustrated in Fig. 3.10(b). The darker circles represent corner-atoms, while the brighter circles represents the center atoms that contribute to the surface. The shaded area is $\sqrt{2}a^2$ and contains 2 atoms. From that it can be deduced that the atom-density at the W(110)-surface is

$$\sigma_{W(110)} = \frac{\sqrt{2}}{a_w^2} \approx 0.141\text{Å}^{-2}. \tag{3.1}$$

The Ir(111) surface is illustrated in Fig. 3.10 (c). The shaded area is $\sqrt{3}a^2/8$ and contains $3/6 = 1/2$ atoms. The surface atom-density of the Ir(111)-surface is thus

$$\sigma_{Ir(111)} = \frac{4}{\sqrt{3}a_{Ir}^2} \approx 0.157\text{Å}^{-2}. \tag{3.2}$$

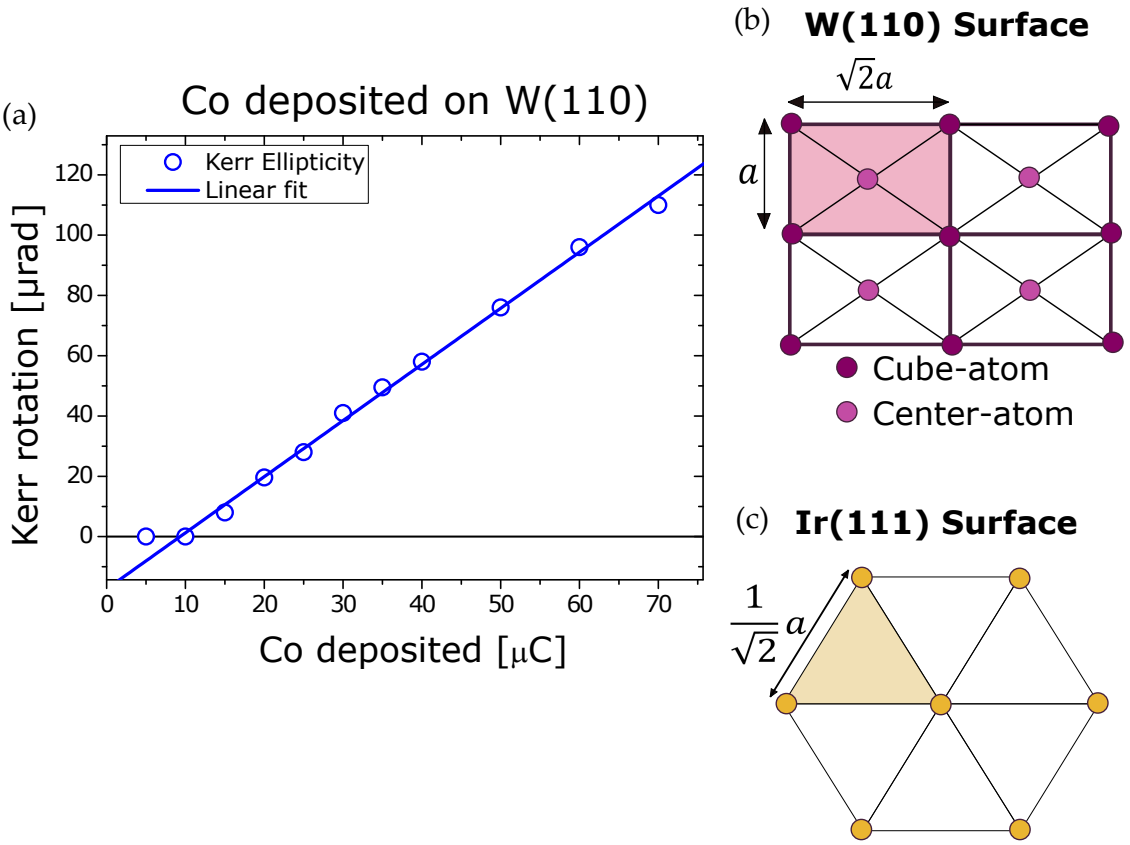

FIGURE 3.10: (a) The Kerr rotation as a function of µC of Co deposited on W(110) with the lab equipment used in this thesis. The point where the linear fit crosses the y-axis, represents 1ML. (b) the surface structure of a W(110) surface. (c) the surface structure of an Ir(111)-surface.

The lattice constant for W is $a_w = 3.165\,\text{Å}$, for Ir it is $a_{Ir} = 3.839\,\text{Å}$. The ratio between the surface particle density of the two surfaces, should be approximately the ratio between the deposited Co per monolayer,

$$\frac{\sigma_{W(110)}}{\sigma_{Ir(111)}} \approx \frac{\text{Co}/ML(W)}{\text{Co}/ML(Ir)} \approx 0.9. \tag{3.3}$$

Following this, approximately 10 µC deposited Co corresponds to one monolayer on the Ir(111) suface, with the instruments used in this thesis.

Chapter 4

Results and discussion

4.1 Out-of-plane magnetization

The MOKE data for different thicknesses of Co grown on the Ir(111) substrate are presented in Fig. 4.1(a). It is clear form the data that a hysteresis loop is first observed at 3 ML film thickness. As more Co is added, from 3 ML to 3.5 ML, the coercivity of the loop decreases. For in-plane magnetization, one would expect the MOKE data to develop in a manner like in Fig. 3.10. In that case a small hysteresis loop would be observed at all thicknesses above 1 ML. It is known that in a longitudinal MOKE geometry, Kerr rotation can be observed also for out-of-plane,

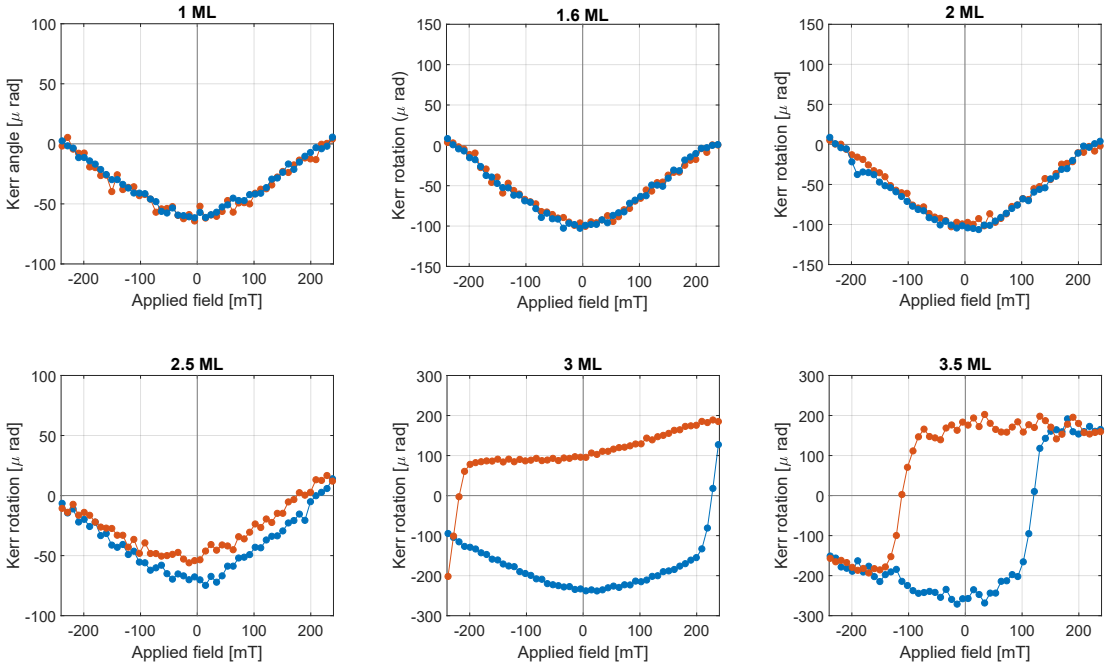

FIGURE 4.1: MOKE hysteresis loops measured for 1-3.5 ML Co grown on the Ir(111) substrate.

polar, magnetization [59]. Generally, the Kerr rotation is much larger for out-of-plane than for in-plane magnetization in such a geometry [1]. Figure 4.1(a) provides a reference about roughly which magnitudes one would expect for a Co film with in-plane magnetization; for a film with a thickness of 3.5 ML, the remanence is about 50 µrad. The measured remanence at 3.5 ML, in the present case, is 219 µrad, which is huge in comparison to the one of the in-plane sample. It is therefore natural to conclude that this is a polar Kerr signal. The measured MOKE signal for 1-2.5 ML may be understood as an indication of a minor loop. This is due to the fact that the coercivity of the loop is far above the reachable fields in our setup, that is limited to applied fields of ±238 mT. It is clear from the 3 ML graph, that the coercivity is at the edge of the field that can be applied by our instrument. It seems that the coercivity of 2.5 ML is larger than that of 3 ML and therefore cannot be properly measured. It is reasonable that the anisotropy increases as the sample

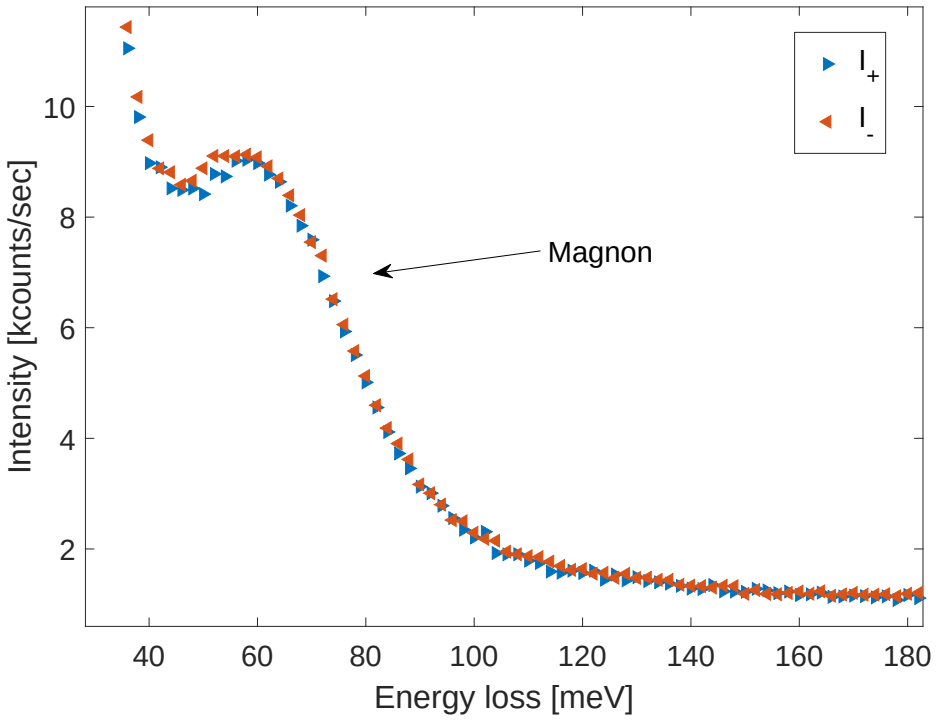

FIGURE 4.2: SPEELS spectra for measured with wave vector transfer $\Delta K = 0.6\,\text{Å}^{-1}$. The blue and red arrows, corresponds to data collected with opposite electron beam polarization. They are polarizations of spin-up (blue) and spin-down (red) orientation in the frame of reference of a sample with in-plane magnetization. It can be seen the magnon excitation peak is not spin resolved. This is a clear indication that the magnetization of the sample is out-of-plane.

[1] It is important to note that the Kerr-rotation is an optical effect and cannot always be directly converted to the total magnetic moment of the magnetism of the sample. The strong polar Kerr rotation does not mean that the magnetization is larger for an out-of-plane easy axis.

thickness decreases. Coercivity is a measure of the system's resistance to become demagnetized - the stronger the magnetic anisotropy the more energy is needed to flip the magnetization and the higher the coercivity. The easy magnetization axis of a sample is determined by a competition between the magneto-crystalline anisotropy and the shape anisotropy. The magneto-crystalline anisotropy is determined by the preferred magnetization direction of the crystalline structure and can favour polar magnetization. The shape anisotropy is determined by the shape of the magnet. For an ultra-thin film, the surface contribution to the magneto-crystalline anisotropy usually tends to rotate the magnetization to the out-of-plane geometry. In contrast, the shape anisotropy prefers an in-plane magnetization direction. As the thickness of the film increases, the influence of the shape anisotropy increases. At a certain thickness the shape anisotropy is the dominating term and the easy magnetization axis will be in-plane. The MOKE data indicate that the Co film has an out-of-plane easy magnetization axis and that the polar anisotropy is reduced as the film thickness increases. This can be seen by the behaviour of coercivity as function of film thickness. One would expect that at some film-thickness the easy direction of the Co film will be in-plane. At that point one would expect that the MOKE data show a behaviour similar to Fig. 3.10(a). A further evidence that the Co film has out-of-plane magnetization is the SPEELS intensity spectra. A typical intensity spectra is shown in Fig. 4.2, for a wavevector transfer $\Delta K = 0.6\,\text{Å}^{-1}$. Our setup is designed to measure in-plane magnetization. The blue arrows, I_+, are the measured electron intensities for an electron beam, polarized in the spin-up direction in the frame of reference of a sample with in-plane magnetization. The red arrows, I_-, are measurements done with the opposite electron beam polarization. It is clear that the magnon-peak [2] is equally well resolved for the two electron beam polarizations. If the sample had in-plane magnetization, there would have been a discrimination between the two polarizations of the beam. For out-of-plane magnetization, however, the sample does not see the electron beam as spin polarized because in the frame of reference of the sample, spin-up and spin-down refers to states orthogonal to the polarization vector of the beam [18]. Spin-up and spin-down as seen in the reference frame of an out-of-plane magnetized film, are equally probable states for an electron beam polarized in the up- or down-direction in the frame of an in-plane magnetized film. Based on the strong evidence from the SPEELS and MOKE measurements, we conclude that the magnetization of a 1.6 ML Co film grown on the Ir(111) substrate is out-of-plane. This is in agreement with Refs. [60–62].

[2] How one can conclude that the peak comes from a spin wave excitation is discussed in 4.2.

4.2 Features of the SPEELS spectrum

Since the SPEELS measurements of Co on Ir(111) are not spin-resolved, a thorough investigation is necessary to identify the magnon excitations in the spectra. There are two main characteristics of the magnon excitation peak, that distinguishes it from peaks originating from phonon excitations and vibrational modes. One feature is that the magnon disperses in a nearly quadratic form, as the wave vector transfer ΔK is varied. Another feature is that the FWHM (full width at half maximum) of a magnon peak is rather large and increases with wavevector.

4.2.1 Development of excitations with changing wave vector

Low energy magnon modes disperse strongly with wave vector q and can be distinguished from other excitations by this feature. The non-spin-resolved SPEELS spectra contains other excitations such as phonon modes and vibrational modes of adsorbates on the Co surface in addition to the magnon modes. It is known that phonon modes in thin magnetic films have energies much lower than that of magnons.

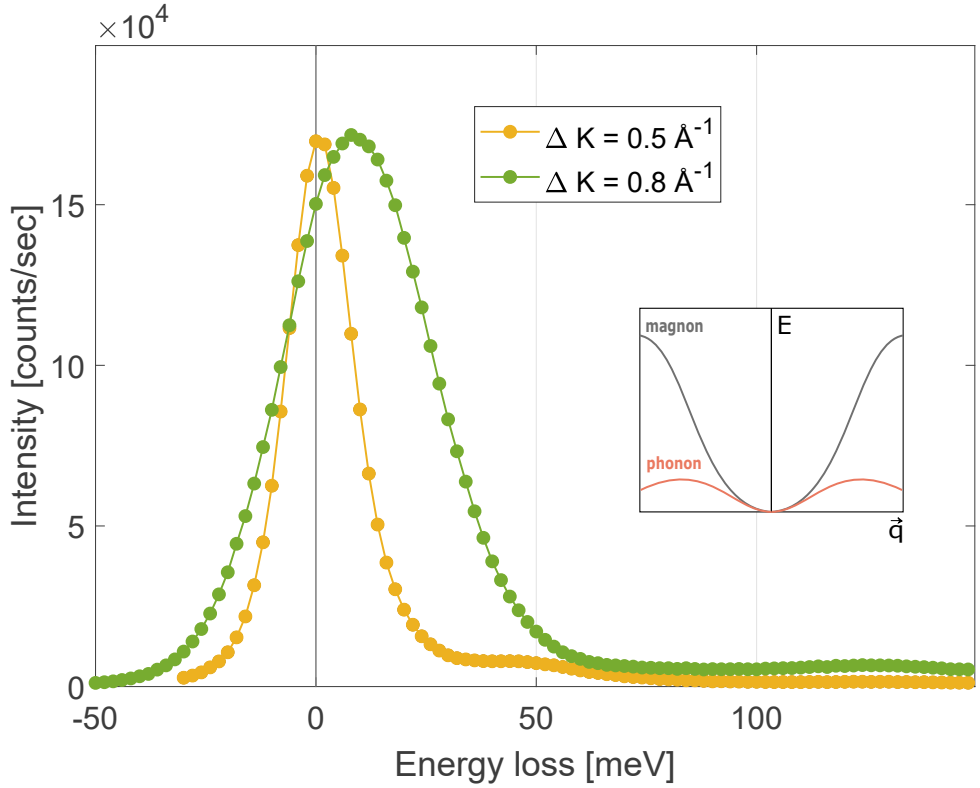

FIGURE 4.3: The quasi-elastic peak for SPEELS measurements with wave vector transfer $\Delta K = 0.5\,\text{Å}^{-1}$ (yellow dots) and $\Delta K = 0.8\,\text{Å}^{-1}$ (green dots). The inset represents a qualitative sketch of the phonon and magnon dispersion curves. The development of the quasi-elastic peak can be explained by the contribution of low energy phonon modes.

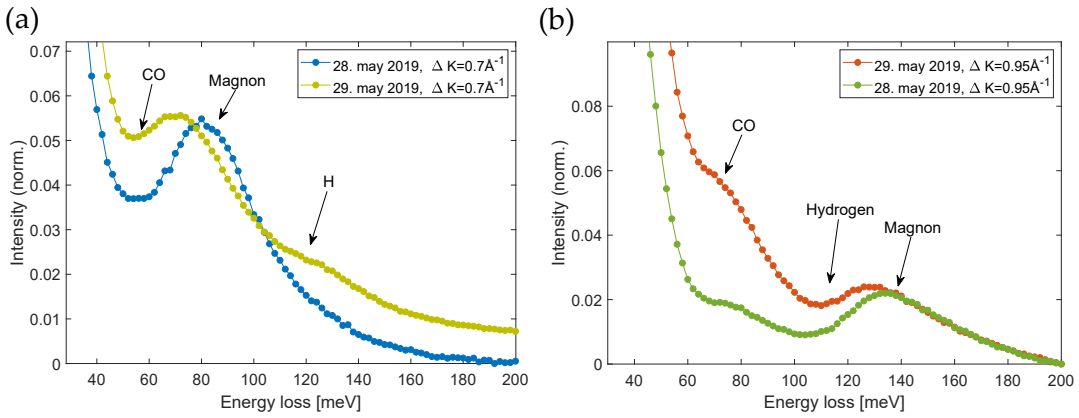

FIGURE 4.4: Normalized SPEELS spectra of wavevector transfer $\Delta K = 0.7\,\text{Å}^{-1}$ (a) and $\Delta K = 0.95\,\text{Å}^{-1}$ (b) measured on the same sample. The blue (green) dots are measurements done the same day as the sample was grown. The yellow (red) dots are measurements done the day after the sample was grown. The intensity of the CO and H adsorbate-peaks have clearly increased as more adsorbates have stuck to the surface over night. In (b), the green spectrum is multiplied by a factor of 0.8 for clarity.

Phonon modes also disperse with wave vector but their energies are so low that their presence first and foremost influence the position of the quasi-elastic peak. This can be seen in Fig. 4.3, where the data from two SPEELS-measurements are plotted together with a qualitative sketch of the magnon and phonon dispersion relations. The yellow dots represent the intensity spectrum for $\Delta K = 0.5\,\text{Å}^{-1}$, the green dots for $\Delta K = 0.8\,\text{Å}^{-1}$. The apparent shape of the quasi-elastic peak is influenced by phonon excitations. At low wavevector transfer the influence is small, because the phonon modes have very low energy. This is accordance with the yellow quasi-elastic peak, that is fairly symmetric and well centered about zero. The phonon dispersion, peaks around the middle of the Brillouin zone. At this point, their energy is high enough to skew the position of the overall peak. The overall peak is then asymmetric with a larger proportion towards positive energy loss, because more phonons are created (loss) than annihilated (gain). This can be seen in the green quasi-elastic peak. The overall peak is asymmetric and moved to the right, due to the presence of phonon peaks.

At higher energies some peaks appear that originate from vibrational modes of adsorbates on the surface. Those modes have flat dispersion relation and therefore do not move considerably with ΔK. The peak intensity of an adsorbate vibrational mode, grows as more adsorbates have stuck to the surface. This can be seen in Fig. 4.4 that show the evolution of the SPEELS spectra as the sample was left over night, for momentum transfers $\Delta K = 0.7\,\text{Å}^{-1}$ [Fig. 4.4(a)] and $\Delta K = 0.95\,\text{Å}^{-1}$, [Fig. 4.4(b)]. The intensity spectra are normalized and in Fig. 4.4(b), the green spectrum

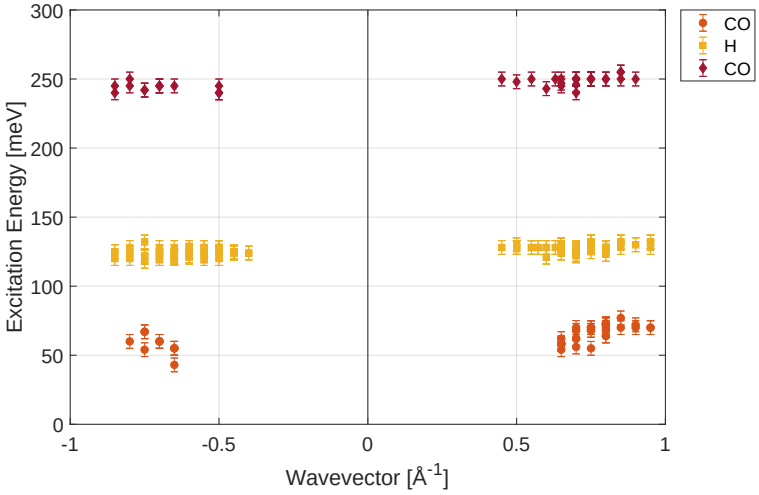

FIGURE 4.5: The measured vibrational modes as function of the wavevector. The lowest (orange) and top (red) mode originate from CO molecules. The middle (yellow) mode is a result of H(H_2) vibrational excitations. All modes show a flat dispersion.

is multiplied by a factor of 0.8 for clarity. In both graphs it is clear that the CO and H peaks have grown over night, while the magnon peak is of the same magnitude. The magnon peak move as the wavevector transfer ΔK is varied, while the adsorbate peaks show no dispersion. It is well documented that adsorbates of CO and H have vibrational modes matching the energies indicated in the figure [63]. It is also expected that residual gases of CO and H are present in the UHV chamber. Based on this, and their flat dispersion, it is clear that these peaks originates from CO and H vibrational excitations. Fig. 4.4 underpin the importance of a clean sample - as the adsorbate peaks rise, the magnon peak becomes less resolved. The measured vibrational mode energies as a function of wave vector is given in Fig. 4.5. The two lowest modes, circle (orange) and square (yellow), are the CO- and H-modes seen in Fig. 4.4. The diamond (red) mode is a higher energy vibrational mode of the CO adsorbate. As all these vibrational modes have fixed positions in the energy loss-spectra, they can easily be distinguished from a magnon mode on a clean sample.

The dispersion of the magnon peak can be seen in Fig. 4.6, that show intensity spectra measured at the same day, with the same sample and electron beam optimization, for wavevector transfers spanning from $\Delta K = 0.5\,\text{Å}^{-1}$ to $\Delta K = 0.8\,\text{Å}^{-1}$. Also in this figure the intensities are normalized. In addition each spectrum is multiplied with a factor to make the comparison clearer - the $\Delta K = 0.8\,\text{Å}^{-1}$ spectrum show for example higher intensities than the $\Delta K = 0.55\,\text{Å}^{-1}$ spectrum, due to this. The dots mark the magnon peak centres. For the spectrum measured at $\Delta K = 0.5\,\text{Å}^{-1}$,

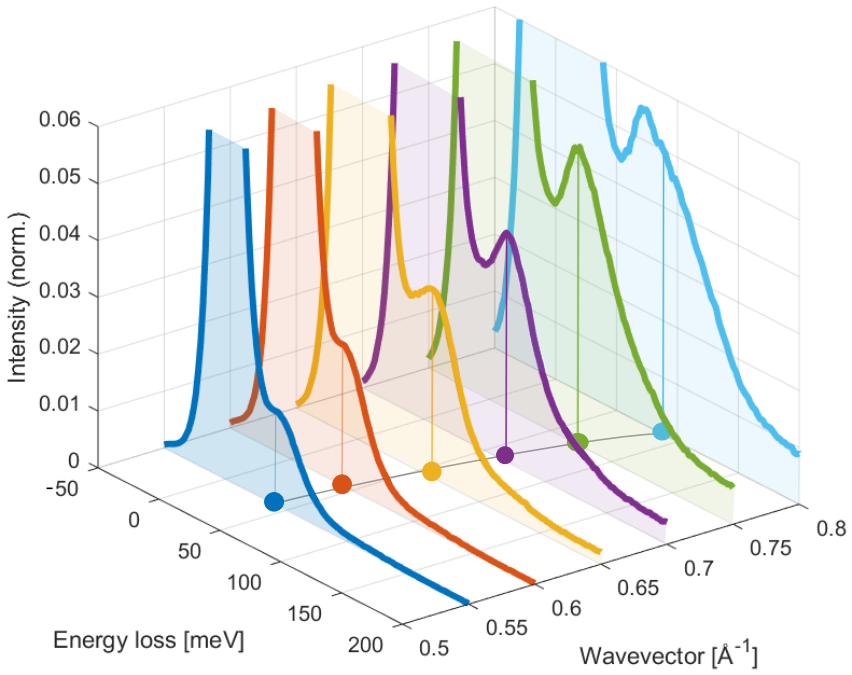

FIGURE 4.6: Intensity spectra measured at the same day, on the same sample and with the same electron beam optimization, for wavevector transfers spanning from $\Delta K = 0.5\,\text{Å}^{-1}$ to $\Delta K = 0.8\,\text{Å}^{-1}$. The intensity is normalized and each spectrum is multiplied with a factor to make the comparison clearer - the $\Delta K = 0.8\,\text{Å}^{-1}$ spectrum show for example higher intensities than the $\Delta K = 0.55\,\text{Å}^{-1}$ spectrum, due to this. Each color represents a wavevector, that can be seen along the y-axis. The dots mark the magnon peak centres. For the spectrum measured at $\Delta K = 0.5\,\text{Å}^{-1}$, it seems that the peak is at slightly smaller energies. This is because the CO vibrational excitation coincides with the magnon peak in this spectrum.

it seems that the peak is at slightly smaller energies. This is because the CO vibrational excitation coincides with the magnon peak in this spectrum. The magnon peak moves about 50 meV as ΔK is varied from $\Delta K = 0.5\text{Å} - 1$ to $\Delta K = 0.8\text{Å} - 1$.

4.2.2 Magnon lifetime

Beside the strong dispersive behavior, a magnon peak broadens with energy. This is again a feature that distinguishes a magnon peak from the vibrational modes present in the non-spin-resolved SPEELS-spectra - vibrational modes do not broaden as strong as magnons. The broadening of the measured intensity peaks, origins from both homogeneous and inhomogeneous broadening effects. Each event of an electron being measured by the channeltron represents an independent random variable.

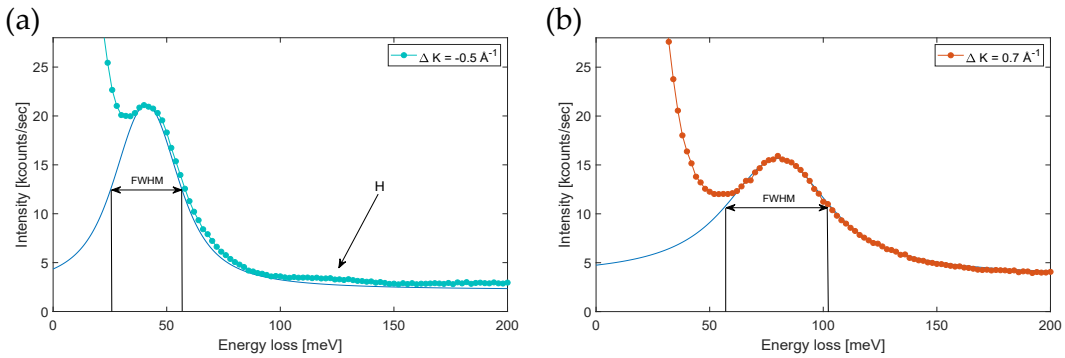

FIGURE 4.7: Intensity spectrum for (a) $\Delta K = -0.5\,\text{Å}^{-1}$ and (b) $\Delta K = 0.7\,\text{Å}^{-1}$ fitted with Voigt profiles. The marked FWHM is of the Voigt peak and increases with wavevector. The Voigt profile in (a) is a convolution of a Gaussian with 16.8 meV FWHM and a Lorentzian with $\Gamma = 25$ meV. The Voigt profile in (b) is a convolution of a Gaussian with 18.2 meV FWHM and a Lorentzian with $\Gamma = 49$ meV. This corresponds to a lifetime of $\tau = 53$ fs in (a) and $\tau = 27$ fs in (b). In (a) the arrow mark the place where the vibrational excitation of adsorbed H on the surface were observed.

The central limit theorem states that the sum of independent, equally distributed, random variables, will be normally distributed as their quantity goes to infinity. The measurements themselves are therefore normally distributed and represent an inhomogeneous broadening. The normal distribution is described by a Gaussian function. The excitations are naturally homogeneously broadened due to Heisenberg's uncertainty principle,

$$\Delta E \Delta t \geq \frac{\hbar}{2} \tag{4.1}$$

that relates the uncertainty in energy, ΔE, and lifetime, Δt. Time and frequency domain are related through Fourier transforms. According to Fermi's Golden Rule a quantum excited state decays exponentially with time, which leads to a Lorentzian distribution of the energy (frequency domain), as the Fourier transform of an exponential decay function is a Lorentzian. In opposite direction, the broadening of the Lorentzian function in energy domain can be used to calculate the lifetime of the excited state. The Fourier transform of a Lorentzian is an exponentially decaying function. Denoting the FWHM of the Lorentzian distribution as Γ, the lifetime

$$\tau = \frac{2\hbar}{\Gamma} \tag{4.2}$$

is defined as the time in which the amplitude of the excited state drops to e^{-1} of its original value. An observed peak in the intensity spectra has a Voigt profile - it is a convolution between Gaussian and Lorentzian distribution functions. The Gaussian distribution represents the instrumental broadening while the Lorentzian

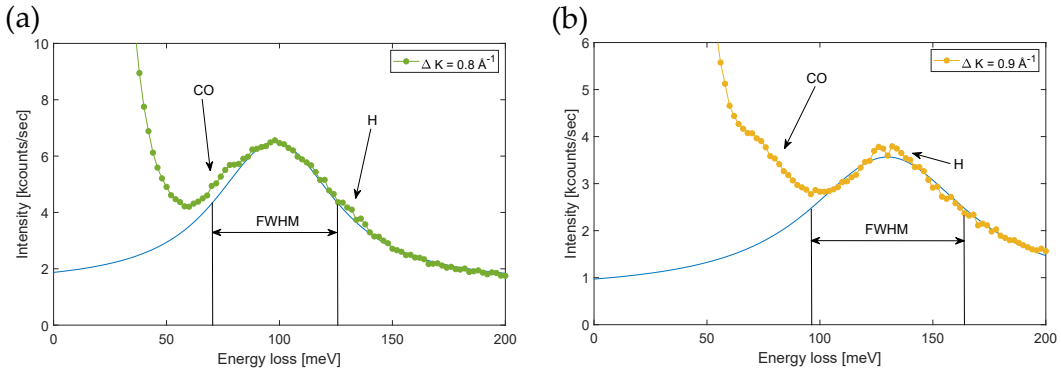

FIGURE 4.8: Intensity spectra for (a) $\Delta K = 0.8\,\text{Å}^{-1}$ and (b) $\Delta K = 0.9\,\text{Å}^{-1}$ fitted with Voigt profiles. The marked FWHM is of the Voigt peak and increase with wavevector. The Voigt profile in (a) is a convolution of a Gaussian with 17.3 meV FWHM and a Lorentzian with $\Gamma = 59$ meV. The Voigt profile in (b) is a convolution of a Gaussian with 17.5 meV FWHM and a Lorentzian with $\Gamma = 78$ meV. This corresponds to a lifetime of $\tau = 22$ fs in (a) and $\tau = 17$ fs in (b). The arrows mark the places where the vibrational excitations of adsorbed CO- and H on the surface is observed.

distribution represents the intrinsic magnon signal. For a Voigt-fit, the linewidth of both the Gaussian and Lorentzian distribution must be determined. The linewidth of the instrumental broadening, the FWHM of the Gaussian distribution, is set to the resolution of the electron beam that is about 15-20 meV, depending on the optimization used during measurement. This is a slight overestimation, due to the phonons influence on the quasi-elastic peak, discussed in Section 4.2.1. The linewidth of the intrinsic magnon signal, Γ, is determined by fitting the Voigt profile to the measured data. As the electron beam resolution is kept at approximately the same

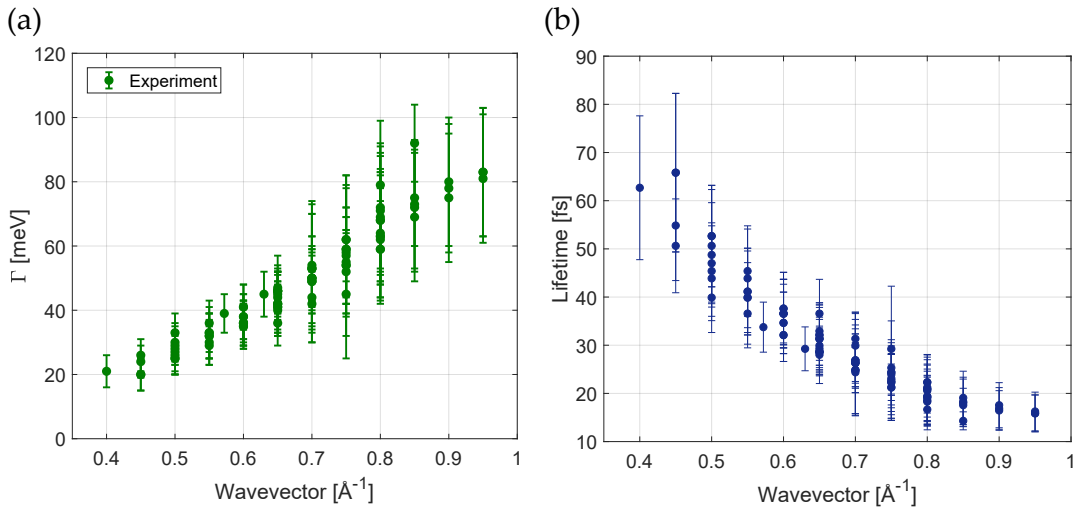

FIGURE 4.9: **(a)** Γ of the Lorentzian in the Voigt-fit of all the magnon peaks measured in this thesis. The uncertainty is given by the uncertainty in linewidth of the fitted peak. **(b)** An estimate of the lifetime of the magnons in (a), calculated with Equation 4.2. The uncertainty is estimated by standard error propagation $\left(\Delta\tau = \Delta\Gamma 2\hbar/\Gamma^2\right)$

value throughout the measurements, it is clear that the broadening of the magnon peaks is due to an increase in Γ. Fig. 4.7 and Fig. 4.8 show magnon peaks, each fitted with a Voigt profile, for $\Delta K = -0.5\,\text{Å}^{-1}$ [Fig. 4.7(a)], $\Delta K = 0.7\,\text{Å}^{-1}$ [Fig. 4.7(b)], $\Delta K = 0.8\,\text{Å}^{-1}$ [Fig. 4.8(a)] and $\Delta K = 0.9\,\text{Å}^{-1}$ [Fig. 4.8(b)]. The electron beam resolution and Γ of each Voigt fit is given in the Figure captions. It is clear that the peak, not only move, but broadens with increasing ΔK. This is again a strong evidence that the measured peak indeed is a magnon excitation. It is the change of magnon lifetime with wave vector that causes the broadening of the magnon peak with increasing wave vector - high energy magnon states have shorter lifetime than magnon states of lower energy. Figure 4.9(a) shows the Γ values extracted from the experimental data in this thesis, as function of the wavevector (absolute value). Fig. 4.9(b) is a plot of the corresponding lifetimes that span from 66-15 fs. The short lifetime of high-energy magnons are mainly due to the dissipation into the Stoner continuum. As discussed in Section 2.2.1 and seen in Fig. 2.2 the spin wave states coincide with the Stoner continuum at high energies. This results in a decay of high-energy magnon states into the available Stoner states. The higher order magnons are in addition influenced by the damping mechanism discussed in Section 2.4.1 [Fig. 2.7]. The additional damping means that higher order magnons have even shorter lifetime than a magnon with the same energy but of lower order.

4.3 Dispersion relation

The main experimental results of this thesis are the measurements of SPEELS spectra for a 1.6 ML thick Co film on an Ir(111)-surface, along the $\bar{\Gamma}$-$\bar{\mathrm{K}}$ direction of the surface Brillouin zone. In the course of this thesis, 93 intensity spectra with visible magnon peaks were collected and analyzed. Each spectrum is a result of 3-21 consecutive scans. The peak position was identified using a Voigt-profile, as discussed in Section 4.2.2.

In order to understand the behaviour of the magnon modes, first-principles calculations within the generalized gradient approximation of the density functional theory (DFT) have been performed in collaboration with Prof. Arthur Ernst (JKU, Linz). The magnon dispersion relation theoretically calculated with this method, has shown very good agreement with experiments for Fe-films [16–18]. For Co-films, it was discovered that the fist-principles calculations overestimate the magnon energies. It has been found that this overestimation is because experimentally probed electronic band structures of Co films cannot be described appropriately within the singe-particle DFT [21, 22]. To obtain better agreement with the experimental results, one should renormalize the majority-spin states of 3d bands towards the Fermi level, keeping the minority-spin states unchanged [20–22]. The need for this renormalization has been attributed to the stronger correlation effects for the majority-spin states. The weakness of the single-particle DFT based approach, is therefore that it overestimates the values of the exchange splitting. This has been taken into account in the first-principles calculation performed in this thesis. Here, the majority bands are renormalized according to magnitudes found for a 3ML Co film grown on a Pt(111)-surface [19], that was discovered to be higher than for a Co(001)- or Ir(001)-surface. As only the majority band is renormalized, the magnitude of the renormalization is directly proportional to the reduction in exchange splitting.

The measured peak energies as a function of the wavevector are represented in Fig. 4.10(a). The results are plotted with the dispersion relation obtained by the first-principles calculations. The colored dispersion relation has been obtained as discussed above. The gray dispersion relation is the result of the first-principles calculations without taking the correlation effects into account. It is clear that the dispersion relation is overestimated compared with the experimental data, with and without considering the correlation effects. In the case where the correlation effects are not taken into account, the overestimation is even higher. This is interesting, as

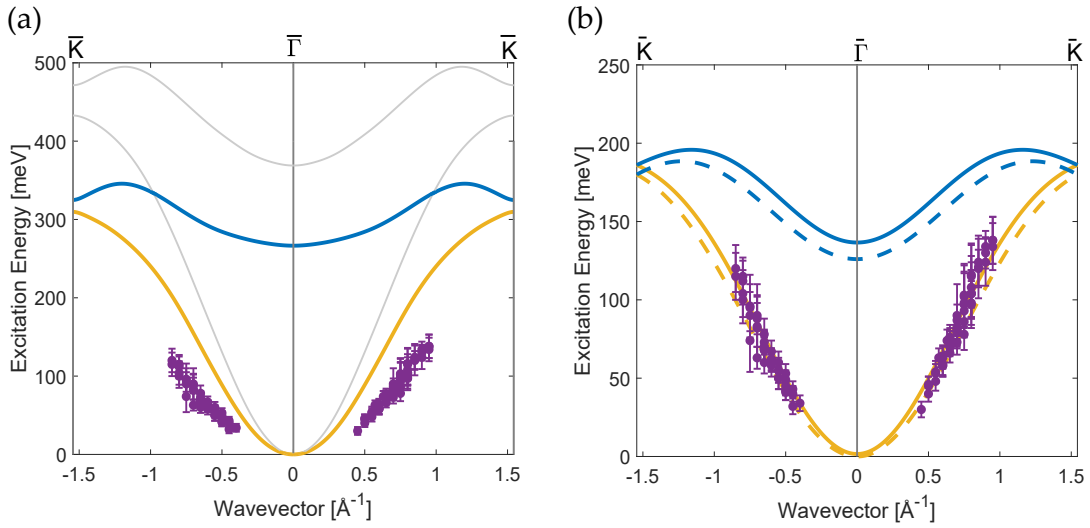

FIGURE 4.10: The measured magnon dispersion relation along the $\bar{\Gamma}$-$\bar{\mathrm{K}}$ direction of the surface Brillouin zone. In **(a)** the experimental data are plotted with dispersion relations calculated in collaboration with Prof. Arthur Ernst (JKU, Linz), based on first principles. The colored dispersion relation is the result of the calculation with correlation effects taken into account. in which the energy of the Co majority band has been renormalized with a magnitude matching the results of earlier research [19]. The gray dispersion relation is the result of the calculation without taking correlation effects into account. In **(b)** the experimental data are fitted with a dispersion relation calculated based on the Heisenberg model with nearest and next nearest neighbor interactions taken into account (solid line). The dashed line is the dispersion relation when only nearest neighbors are considered. The exchange constants used in this fit are $J_{\parallel} = 6.5\,\mathrm{meV}$ and $J_{\perp} = 10.5\,\mathrm{meV}$ for nearest neighbor interaction, and $J_N^{\parallel} = 0.5\,\mathrm{meV}$ and $J_N^{\perp} = 1.3\,\mathrm{meV}$ for next nearest interactions. The uncertainty in each data point is estimated through the uncertainty of the peak-fit. The uncertainty is strongest for wavevectors near 0.75 Å, because there the magnon peak coincides with the CO- and H vibrational modes discussed in Section 4.2.1.

it is in agreement with earlier work, stating that the electronic band structures of Co films cannot be described appropriately within the singe-particle DFT.

To provide an estimation of the appropriate values of the exchange constants, a simple calculation was done to fit the the experimental data according to the Heisenberg model as discussed in Section 2.4. The resulting dispersion relation is plotted with the experimental data in Fig. 4.10(b). The dashed line is the dispersion relation calculated considering only nearest neighbor interactions. The solid line is the resulting dispersion relation when also next nearest neighbor interactions are taken into account. This calculation was conducted with the (incorrect) assumption that the exchange constants are the same for both layers. In reality, the exchange constants of the interface layer are lower than those of the surface layer. This is due to the hybridization of the electronic states of the ferromagnetic interface layer with those of the substrate. The degeneracy near the Brillouin zone boundary in this model is due to the fact that an isotropic exchange interaction is assumed. In the first-principles calculations, the fact that the exchange constants in different layers are different has been properly taken into account. This can clearly be seen in 4.10(a) where the degeneracy of the magnon bands is lifted. The calculations based on the Heisenberg model produce a dispersion relation that fit the data rather well. This is because the values used for this model represent average values of exchange constants of the two layers. Here the exchange constants are set to $J_{\parallel} = 6.5\,\mathrm{meV}$ and $J_{\perp} = 10.5\,\mathrm{meV}$ for nearest neighbor interaction, and $J_N^{\parallel} = 0.5\,\mathrm{meV}$ and $J_N^{\perp} = 1.3\,\mathrm{meV}$ for next nearest interactions. $J_{\parallel}$ represents the exchange interaction within each layer. $J_{\perp}$ represents inter-layer exchange interactions. As discussed in Section 2.4, is $J_{\perp} > J_{\parallel}$ because the distance to the nearest neighbors in the neighboring layer is less than the distance to the nearest neighbor in the same layer. The exchange constants equivalent to $J_{\parallel}$ and $J_{\perp}$, in the first-principles calculation are $J_{\parallel} = 7\,\mathrm{meV}$ for nearest neighbor interactions on the interface (bottom) layer and $J_{\parallel} = 10\,\mathrm{meV}$ for nearest neighbor interactions on the surface (top) layer. The value of the inter-layer exchange constant is $J_{\perp} = 13.3\,\mathrm{meV}$. These are all higher than the values obtained by our simple fitting based on the Heisenberg model.

While going through the SPEELS-spectra, analyzing them, a weak signal that look like a higher energy magnon-mode was discovered. The signal is observed in the SPEELS-spectra presented in Fig. 4.11 for the wave vector transfers $\Delta\mathrm{K} = 0.6\,\mathrm{\AA}^{-1}$, $\Delta\mathrm{K} = 0.7\,\mathrm{\AA}^{-1}$ and $\Delta\mathrm{K} = 0.9\,\mathrm{\AA}^{-1}$. The orange Voigt-peak is the fitted magnon of mode $n = 0$ (n represents the magnon quantum number). The grey peaks are the Voigt-fits of the CO- and H vibrational modes discussed in Section 4.2.1. The

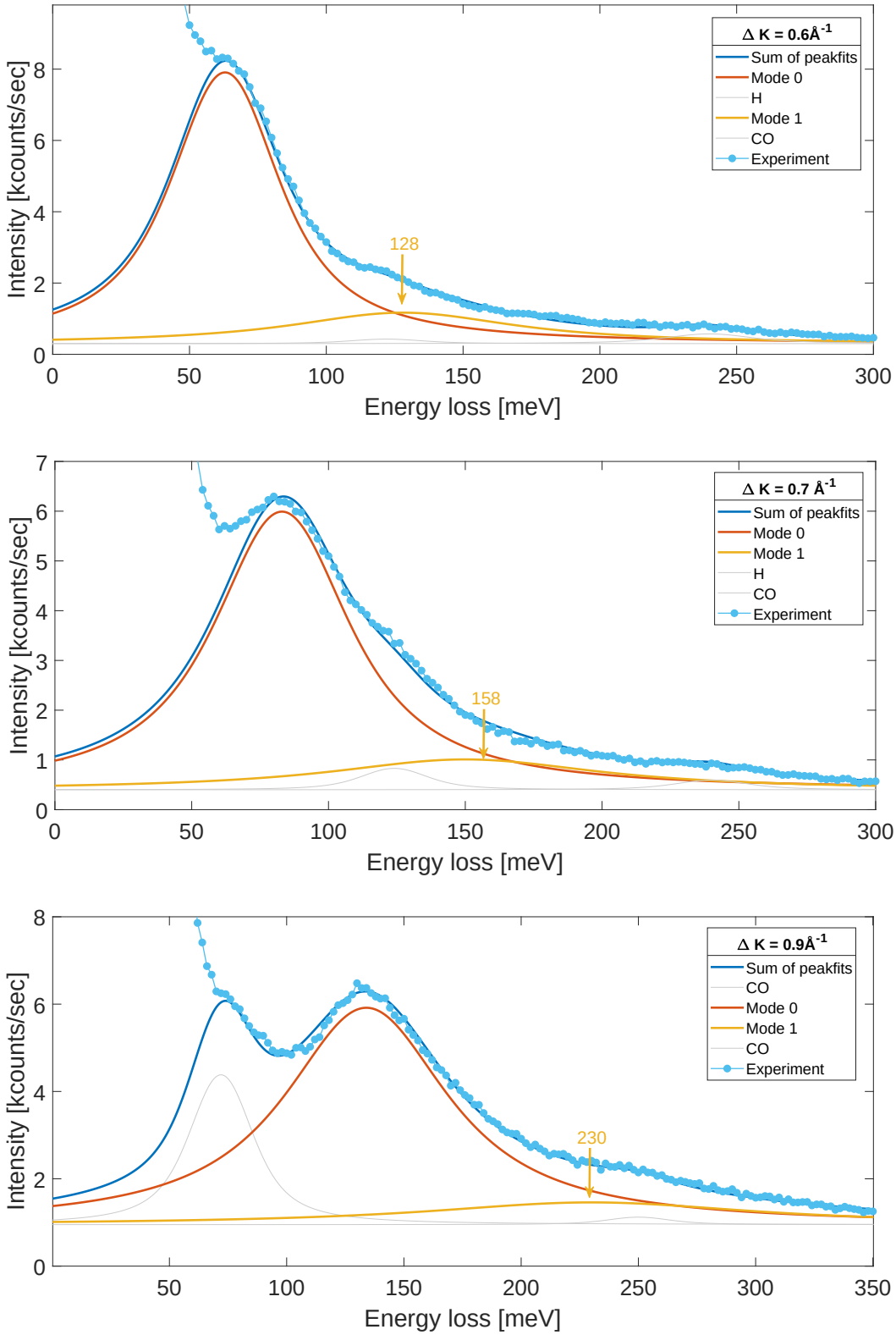

FIGURE 4.11: SPEELS intensity spectra for three different ΔK. The orange Voigt-fit is of magnon mode 0. The yellow Voigt-fit may be of a potential magnon mode 1. The grey peaks are Voigt-fits for the vibrational modes discussed in Section 4.2.1. In the top spectra of $\Delta K = 0.6\,\text{Å}^{-1}$, the yellow peak is centered at an energy loss of (128 ± 15)meV. In the middle, $\Delta K = 0.7\,\text{Å}^{-1}$-spectra, the peak has moved to an energy loss of (158 ± 20)meV. For the bottom, $\Delta K = 0.90.9\,\text{Å}^{-1}$-spectra, the peak has moved further to an energy loss of (230 ± 25)meV.

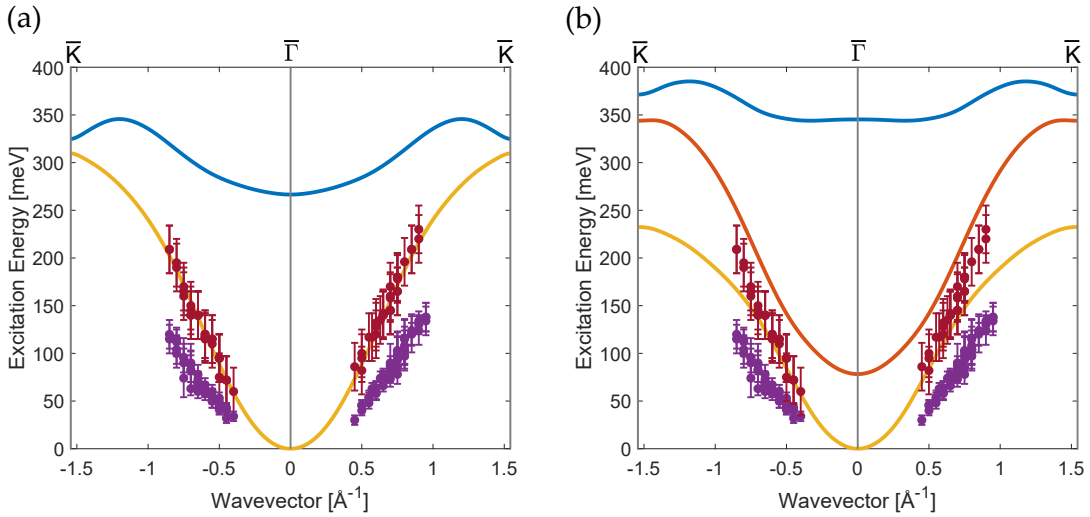

FIGURE 4.12: The measured magnon dispersion relation along the $\bar{\Gamma}$-$\bar{K}$ direction of the surface Brillouin zone. The data are plotted with dispersion relations calculated in collaboration with Prof. Arthur Ernst (JKU, Linz), based on first principles, for a bilayer system (a) and a trilayer system (b). The purple dots are the experimental data from the first magnon peak. The red dots are the experimental data from the second magnon peak. The uncertainty in each data point is estimated through the uncertainty of the peak-fit.

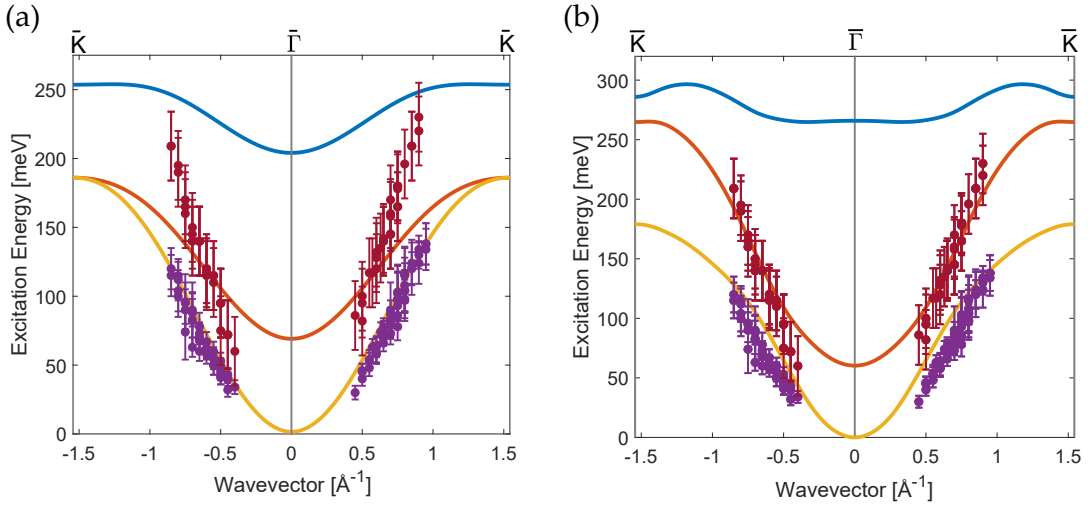

FIGURE 4.13: The measured magnon dispersion relation along the $\bar{\Gamma}$-$\bar{K}$ direction of the surface Brillouin zone. The experimental data are plotted with the dispersion relation of a trilayer system calculated by the use of our simple Heisenberg model (a). In part (b) is the dispersion relation calculated in collaboration with Prof. Arthur Ernst (JKU, Linz), based on first principles, multiplied with a factor of 0.77. The factor was extracted from a comparison between the exchange constants used in the original calculation and the exchange constants extracted from the simple Heisenberg-fit seen in (a). The purple dots are the experimental data from the first magnon peak. The red dots are the experimental data from the second magnon peak. The uncertainty in each data point is estimated through the uncertainty of the peak-fit.

yellow peak is a Voigt-fit to the magnon peak discovered. The blue curve is the sum of the fitted peaks and match well with the experimental data points (light blue). Without the yellow magnon peak, there would be a large gap between the blue line and the experimental data points - the fit would not match the experimental data very well. The peak behaves like a magnon, as it disperses with wavevector and has a broad linewidth. It is, as discussed in Section 4.2.2, expected that the higher order magnon modes exhibit a shorter lifetime. The broadening of the peak, and its low intensity, makes it hard to detect. The peak is not seen in all the 93 SPEELS-spectra in which the magnon of mode $n = 0$ (orange peak) is resolved. In some measurements the signal is so weak that is hard to detect. However, even though the signal is weak, it is possible to see in 63 of the 93 SPEELS-spectra that have been analyzed. From these 63 SPEELS-spectra data points have been extracted to get an estimation of the behaviour of this peak. When plotted with the dispersion relation based on first-principles calculations, one discovers that the second magnon peak fits very well with the $n = 0$ magnon mode. This can be seen in Fig. 4.12(a), where the red data points are the measured energies of the second magnon peak.

The presence of the second magnon mode in the SPEELS intensity spectra, in the unexpected energy region, indicates that the sample is no longer a flat film composed of only bilayers. It also contains patches with various thicknesses. Since we have grown 1.6 ML of Co, one would naturally think that the film is composed of mainly bilayer Co. However, the dispersion relation of this higher order magnon mode indicates that there are patches of more than two layers. The purple and red data points represents the dispersion relation of magnon modes with different quantum number. The magnon mode with quantum number $n = 1$ in the bilayer system is rather flat, and clearly distinguishable from the magnon mode with quantum number $n = 0$. The existence of two magnon modes that have so similar dispersion relations, is a clear evidence that the Co film is not strictly of mono- and bilayer structure (no Frank-van der Merwe growth). To get a better understanding of the system, first-principles calculations were performed, in the same manner as described above, for a trilayer system (calculations are performed by Prof. Arthur Ernst, JKU, Linz). The resulting dispersion relation, together with the experimental data are presented in Fig. 4.12(b). It is apparent that the dispersion relation is overestimated also in the present case, similar to the one of the bilayer system. A calculation for a trilayer system has been made in accordance to our Heisenberg model. This calculation can be seen in Fig. 4.13(a), plotted with the data points. Though the simple Heisenberg model was efficient to fit the data in the case of a bilayer system, it is not as straightforward in the trilayer-case. The trilayer system is more complex than the bilayer

one, and when considering modes with higher quantum numbers it is important to consider each layer individually. The exchange constants are very different in each layer. As the interface and surface layers are treated equally in this calculations, the degeneracy, discussed above for the bilayer system, is also present here. If the interface and surface layers were treated unequally, the dispersion relation, particularly of the $n = 1$ magnon mode, would have had a shape similar to the dispersion relation in Fig. 4.12(a). Due to the complexity and the large number of unknown variables, we have not used this approach in this thesis.

The fit based on the Heisenberg model, for the trilayer system could be useful, even if the shape of the modes with higher energy are not realistic. When looking at Fig. 4.12, one could assume that the red data points could eventually originate from the $n = 0$ magnon mode in the bilayer system, they could also originate from the $n = 1$ mode of the trilayer system which in the calculations, the energies are overestimated. This is in line with the fact that the purple data points, which could eventually correspond to the $n = 0$ mode of the trilayer system, are also lower in energy compared to the calculation. Putting these arguments together one may conclude that the calculations for the trilayer system overestimates all the magnon bands.

Comparing the value of the exchange constants to those estimated using our simple Heisenberg model, one realizes that the exchange constants in the first-principles calculations are overestimated by a factor 1.3. Considering this factor, one obtains the dispersion relation shown in 4.12(b), which explains both the $n = 0$ and $n = 1$ magnon modes of the trilayer system rather well. In order to provide an estimation of the exchange constants, the nearest neighbor inter- and intra-layer exchange parameters, after considering the factor of 1.3, are presented in Table 4.1.

The experimental data provides evidence that the Co film consist of patches of three and two atomic monolayers. The strongest magnon signal (purple data points) originate from the magnon mode with quantum number $n = 0$ of a trilayer structure, seen in Fig. 4.13(b). The weak magnon signal (red data points) could originate

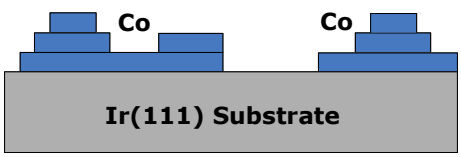

FIGURE 4.14: Co growth with islands of of 1-3 ML of difference size spread on the Ir(111) substrate.

	Interface layer	Middle layer	Surface layer
$J_{\parallel}$ [meV]	4.8	6	8.2
$J_{\perp}$ [meV]	5.2	5.2/11.8	11.8

TABLE 4.1: An estimation of the nearest neighbor exchange constants of the trilayer system, based on an comparison between the values obtained in the first-principles calculations and the fit to the experimental data.

from the $n = 0$ magnon mode of the bilayer structure [Fig. 4.12(a)] as well as the $n = 1$ magnon mode of the trilayer structure [Fig. 4.13(b)]. The fact that the strongest signal originates from patches of trilayer thickness, could be an indication that the film is grown in a Vollmer-Weber manner with islands of three layers. The weak signal from the bilayer structure could indicate that this signal comes from smaller areas of two layers that are also present on this film. Figure 4.14 provides a qualitative sketch of how the structure could look like. The trilayer dispersion relation calculated by first-principles had to be multiplied by a factor 0.77 in order to fit the experimental data. This could very well be due to the complexity of the surface growth structure. The trilayer patches could grow in either fcc or hcp stacking. In all the calculations discussed here, it was assumed that the Co film grows in an fcc-like manner. A potential presence of hcp structures would only affect the trilayer dispersion relation. This matter could be further investigated for example by the use of STM (scanning tunneling microscope). In the calculations based on first-principles, it was assumed that the inter-layer distance of the film was 2.02 Å between consecutive layers of Co and 2.10 Å between the first Co layer and the substrate. In a real sample this values may differ. In particular would a smaller distance between the first Co layer and the Ir substrate influence the exchange interaction so that the exchange constants of this layer would be smaller.

4.4 Antisymmetric exchange interaction

The antisymmetric exchange interaction, the DM-interaction, is of much lower magnitude than the symmetric, Heisenberg exchange interaction. It is therefore hard to make measurements sensitive enough to measure its influence. In a sample with strong DM-interaction, the dispersion relation of the magnon excitation energy is asymmetric with respect to wavevector. The excitation energy is therefore different comparing the spectra for $+\Delta$K to those of $-\Delta$K. The DM-interaction is a result of spin-orbit coupling and the absence of inversion symmetry in the system. An ultrathin film has broken inversion symmetry. Grown on a heavy element substrate, like Ir, one would expect the DM-interaction to be present. Particularly if there are strong interactions between the film and substrate. As discussed in Section 2.1,

and seen in Eq. (2.4), one expects a sinusoidal behaviour of the energy shift due to the DM-interaction. The energy shift is expected to be highest for intermediate wave-vectors.

As the DM-interaction is very weak in comparison to the Heisenberg exchange interaction, it is challenging to measure it. To be able to attribute a change in peak-energy to the DM-interaction, measurements for $\pm\Delta$K must be done at the same day with the same sample. Preferably the beam optimization should be the same for both measurements as well. To preform a measurement on both the plus and minus side with the same beam optimization is often a bit challenging. Often a beam optimization that works well for positive wave vectors has less resolution for negative wave vectors and vice versa. There are therefore not many measurements in which the same beam optimization has been used for both positive and negative wavevector, but there are some. In total, 16 sets of $\pm\Delta$K measurements were done, and 7 of those sets are measured with the same beam optimization for both the plus and minus side. Some selected data sets with $\pm\Delta$K measurements are shown in Figures 4.15 and 4.16. The intensity specta are measured with the same sample, on the same day, with the same electron beam optimization for $\Delta K = \pm 0.5\,\text{Å}^{-1}$, $\Delta K = \pm 0.6\,\text{Å}^{-1}$ and $\Delta K = \pm 0.8\,\text{Å}^{-1}$. The $\Delta K = \pm 0.7\,\text{Å}^{-1}$ set was measured with the same sample, at the same day, but with a slightly different electron beam optimization. The orange data points are from the positive ΔK measurements, while

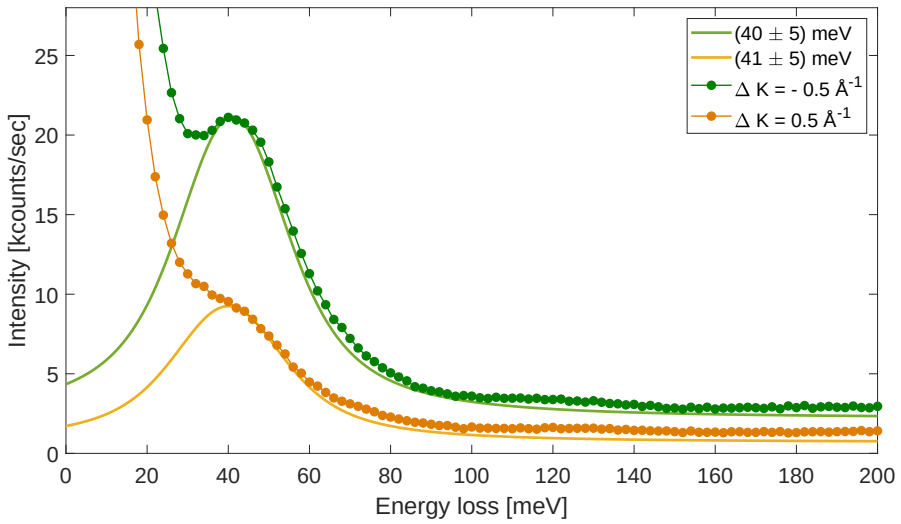

FIGURE 4.15: SPEELS intensity spectra for $\Delta K = \pm 0.5\text{Å}^{-1}$,taken with the same sample, at the same day and with the same electron beam optimization. The experimental data are shown by solid dots and the fits based on Voigt profiles are shown by solid lines. The green plots and curve are the data set and Voigt-fit from the negative side, while the orange and yellow plot and Voigt-fit are from the positive side.

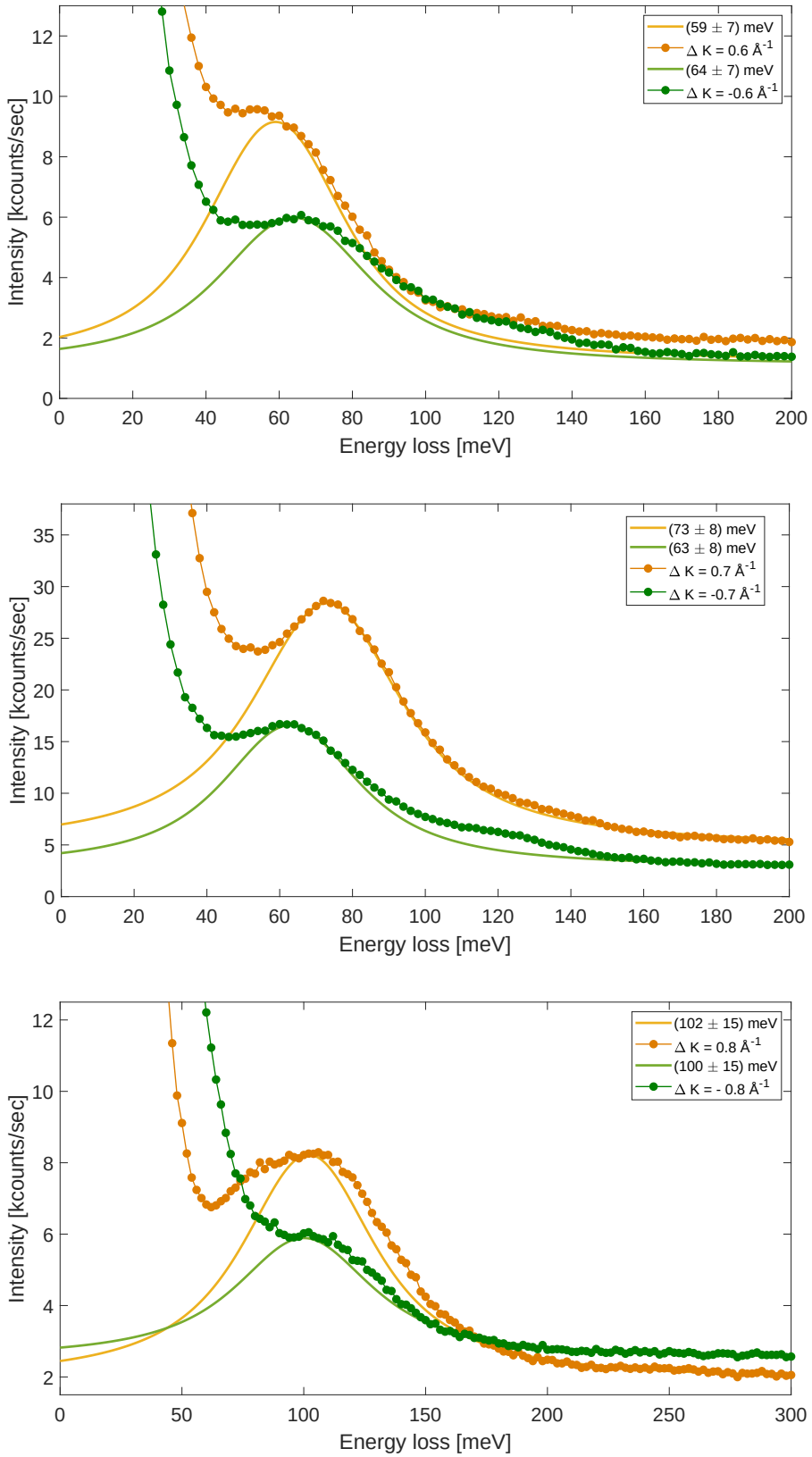

FIGURE 4.16: SPEELS intensity spectra for $\Delta K = \pm 0.6\,\text{Å}^{-1}$(top), $\Delta K = \pm 0.7\,\text{Å}^{-1}$(middle) and $\Delta K = \pm 0.8\,\text{Å}^{-1}$(bottom). Each $\pm\Delta K$-set is taken with the same sample at the same day. The $\Delta K = \pm 0.6\,\text{Å}^{-1}$ and $\Delta K = \pm 0.8\,\text{Å}^{-1}$ sets were in addition measured with the same electron beam optimization. The green plots and curve are the data set and Voigt-fit from the negative side, while the orange and yellow plot and Voigt-fit are from the positive side.

the green data points are from the negative ΔK measurements. The data sets are fitted with a Voigt-peak and the centre of the peaks is given in each Figure legend. In the $\Delta K = \pm 0.5\,\text{Å}^{-1}$ set, no significant movement of the peak is seen. This is as expected, as the energy asymmetry due to DM interaction is small for low wavevector. In the $\Delta K = \pm 0.6\,\text{Å}^{-1}$ and the $\Delta K = \pm 0.7\,\text{Å}^{-1}$ sets, a shift is observed. In the $\Delta K = \pm 0.6\,\text{Å}^{-1}$ set, the peak measured at negative ΔK is at a higher energy than the peak measured at positive ΔK. In the $\Delta K = \pm 0.7\,\text{Å}^{-1}$ set, a shift in the opposite direction is observed. In the $\Delta K = \pm 0.8\,\text{Å}^{-1}$ there is again no significant shift. It could be that the shifts observed in the $\Delta K = \pm 0.6\,\text{Å}^{-1}$ and $\Delta K = \pm 0.7\,\text{Å}^{-1}$ sets originates from the DM-interaction but it is hard to conclude based on these data only.

Figure 4.17 is a plot of the excitation energy differences from each of the 16 data sets sets of $\pm\Delta$K measurements done in this thesis. The excitation energy difference is here defined as the movement of the peak measured at negative ΔK relative to the peak measured at positive ΔK, that is

$$\Delta E = E(-\Delta K) - E(+\Delta K). \tag{4.3}$$

The blue dots in the figure are data points from the sets where $\pm\Delta$K have been measured at the same day with the same sample. The yellow dots are data points from sets where $\pm\Delta$K have been measured the same day, with the same sample and with the same electron beam optimization. The data set as a whole, show a slight tendency towards negative excitation energy difference. All of the blue data points indicate that there is a negative shift. Some of the yellow data points are on the positive side, but at very small magnitudes. The deviation from zero is largest for wavevectors above $\Delta K = \pm 0.6$. It could very well be that this is due to the stronger DM-interaction at those wavevector transfers.

It is hard to make a clear conclusion based on these data. Some measurements show that at intermediate wavevecotrs there is some effect, but due to the broad magnon spectra it is hard to quantify. In order to quantify the effect, it would be necessary with a spin-resolved signal. With our SPEELS-setup, this would be possible to obtain by growing a thicker Co film. The thicker film would have neither in-plane nor out of plane magnetization and the SPEELS signal would be partially spin-resolved. Such a measurement could provide useful insights to the nature of this phenomena.

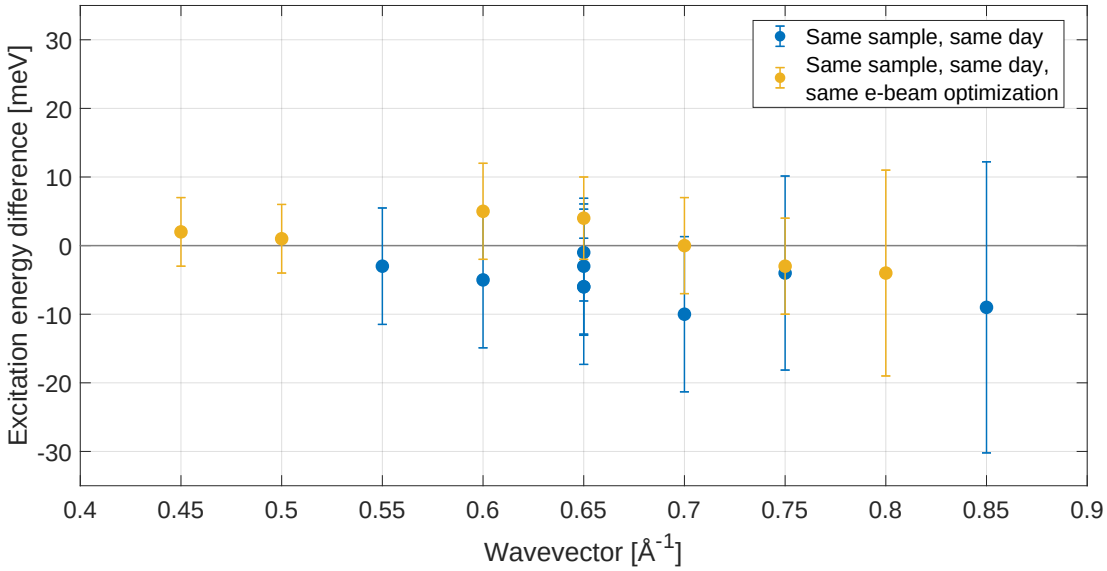

FIGURE 4.17: The measured excitation energy difference between $\pm\Delta$K, as function of wavevector. The excitation energy difference is calculated as $E(-\Delta\text{K}) - E(+\Delta\text{K})$. The blue dots are data points from sets where $\pm\Delta$K have been measured at the same day with the same sample. The orange dots are data points from sets where $\pm\Delta$K have been measured the same day, with the same sample and with the same electron beam optimization. The uncertainty is estimated through the standard uncertainty propagation of the peak-uncertainties.

Chapter 5

Conclusion

In this thesis the SPEELS-spectra of a 1.6 ML thick Co film grown on an Ir(111) substrate have been investigated. Throughout the work of this thesis 93 intensity spectra with visible magnon peaks were collected and analyzed. Each spectra is a result of 3-21 consecutive scans.

The magnetization of the Co film was found to be perpendicular to the surface. This was confirmed by MOKE measurements, showing a polar Kerr rotation. This fact was further confirmed by our SPEELS measurements, in which we observe the magnon excitation peak in both spin channels.

Magnon peaks could be identified in the non-spin-resolved SPEELS spectra. Their peaks could be distinguished from peaks originating from excitations of H and CO adsorbates based on their dispersion relation and their broadening as function of the wavevector.

The magnon spectra were analyzed as a function of wavevector along the $\bar{\Gamma}$-$\bar{\mathrm{K}}$ direction of the surface Brillouin zone. A careful investigation of the spectra revealed a higher order magnon peak. This peak was observed in an energy region in which one would not expect to observe the $n = 1$ magnon mode of a Co bilayer. In contrast to the almost flat dispersion relation to the $n = 1$ magnon mode expected for a bilayer, this mode showed a strong dispersion relation, indicating that the Co film is not only composed of mono- or bilayer regions. The magnon dispersion relation of the system was also theoretically analyzed by the use of two methods. Calculations based on first-principles within the generalized gradient approximation of the DFT, were conducted in collaboration with Prof. Arthus Ernst (JKU, Linz). These calculations were performed for both a bilayer and a trilayer fcc-system. Calculations based on a simple Heisenberg model, taking nearest and next nearest neighbor interactions into account, were performed in order to estimate the effective interatomic exchange

constants.

It was found that the first-principles calculations overestimate the energies of the magnon bands. The overestimation was even higher when correlation effects were not taken into account. This is in agreement with earlier work, stating that the electric band structures of Co films cannot be described appropriately within the single-particle DFT.

When the experimentally measured dispersion relation was compared with the results of calculations based on first-principles, for the trilayer and bilayer system, it was found that the strongest magnon signal originates from the $n = 0$ magnon mode of the trilayer system. The second magnon signal could originate from the $n = 0$ mode of the bilayer structure as well as the $n = 1$ mode of the trilayer structure. The fact that the larger intensity is observed for the first magnon signal, could be an indication that the film is grown in a Vollmer-Weber manner, with islands of three layers.

Furthermore, it was observed that the trilayer dispersion relation based on first-principles calculations, overestimates the energies of the magnon bands. In order to understand the origin of this overestimation, the measured dispersion relation for the lowest energy magnon mode was fitted by calculations based on a simple Heisenberg model, taking only isotropic exchange interactions into account. This calculations could provide an estimate of the average values of the exchange constants of the three layers. Comparing the values obtained through this fit, with the exchange constants in the first principles calculations, it was found that they are overestimated by a factor of 1.3. Considering this factor, the dispersion relation calculated for the trilayer system, based on first principles, matches rather well to the experimental data. Based on this analysis the values of the exchange constants were estimated to be $J_{\parallel}^{i} = 4.8\,\mathrm{meV}$, $J_{\parallel}^{m} = 6\,\mathrm{meV}$ and $J_{\parallel}^{s} = 8.2\,\mathrm{meV}$, where $J_{\parallel}^{i}$, $J_{\parallel}^{m}$ and $J_{\parallel}^{s}$ represent the values of the intralayer exchange constants in the interface, middle and surface layer, respectively. For interlayer exchange, the exchange constants were estimated to be $J_{\perp}^{im} = 5.2\,\mathrm{meV}$ and $J_{\perp}^{ms} = 11.8\,\mathrm{meV}$ where $J_{\perp}^{im}$ denotes the interlayer exchange constant between the interface and the middle layer, while $J_{\perp}^{ms}$ denotes the exchange between the middle and the surface layer.

The overestimation of the magnon band energies in the trilayer dispersion relation, based on first principles, is very likely due to the complexity of the structure. Moreover, one has to consider that the trilayer patches can in principle grow in either

fcc or hcp stacking. The potential presence of hcp structures would only affect the trilayer dispersion relation. The inter-layer distances, that were considered as the input of the first principles calculations, could also be different in a real sample.

A series of measurements were performed with the aim to measure the antisymmetric exchange interaction, the DM-interaction of the sample. These measurements were carried out on the same sample, at the same day to ensure the highest level of precision. In total 16 data sets with $\pm\Delta$K were collected, and 7 of those sets were measured not only on the same sample, at the same day, but also with the same e-beam optimization. The data sets were investigated to quantify the energy asymmetry of $\Delta E = E(-\Delta\text{K}) - E(+\Delta\text{K})$. A slight tendency towards negative ΔE was observed, in particular for intermediate wavevectors. However, due to the broad magnon spectra, it is difficult to quantify the value of the DM-interaction. Such an effect can eventually be better investigated in a sample in which one observe a spin resolved signal.

This work provides some insights into the magnetic nature of ultrathin Co films grown on an Ir(111)-surface as well as the complex surface structure of such a film. The results are in agreement with predictions based on previous research on Co films. In particular does the film show similar magnetic properties as seen in a 3 ML Co film grown on a Pt(111)-surface [19]. To fully understand the structure and magnetic properties of such a system more research must be done. Spin-resolved measurements could provide more insight into the magnetic properties. The film structure could be investigated by STM [64].

Bibliography

1. Sandstad, J. H. *Norwegian Encyclopedia* https://snl.no/magnet. Accessed: 31. august 2019.
2. Stöhr, J. & Siegmann, H. C. *Magnetism: From Fundamentals to Nanoscale Dynamics* ISBN: 3540302824 (Springer, 2006).
3. Ørsted, H. C. *Selected Scientific Works of Hans Christian Orsted* ISBN: 0691043345 (Princeton University Press, 1998).
4. Maxwell, J. C. Dynamical Theory of the Electromagnetic Field. *Phil. Trans. R. Soc. Lond.* **155** (1865).
5. Maxwell, J. C. Experimental relations of gold (and other metals) to light. *Phil. Trans. R. Soc. Lond.* **147** (1857).
6. Ampere, A.-M. *Théorie Mathématique Des Phénomènes Électro-Dynamiques: Uniquement Déduite de l'Expérience (French Edition)* ISBN: 0270926216 (Wentworth Press, 2018).
7. Pauli, W. Über den Zusammenhang des Abschlusses der Elektronengruppen im Atom mit der Komplexstruktur der Spektren. *Zeitschrift für Physik* **31,** 765–783. ISSN: 0044-3328 (1925).
8. Dirac, P. A. M. & Fowler, R. H. The quantum theory of the electron. *Proceedings of the Royal Society of London. Series A, Containing Papers of a Mathematical and Physical Character* **117,** 610–624 (1928).
9. Dirac, P. A. M. & Fowler, R. H. The quantum theory of the Electron. Part II. *Proceedings of the Royal Society of London. Series A, Containing Papers of a Mathematical and Physical Character* **118,** 351–361 (1928).
10. Uhlenbeck, G. E. & Goudsmit, S. Ersetzung der Hypothese vom unmechanischen Zwang durch eine Forderung bezüglich des inneren Verhaltens jedes einzelnen Elektrons. *Naturwissenschaften* **13,** 953–954 (1925).
11. Uhlenbeck, G. E. & Goudsmit, S. Spinning Electrons and the Structure of Spectra. *Nature* **117,** 264–265 (1925).
12. Khitun, A., Bao, M. & Wang, K. L. Magnonic logic circuits. *Journal of Physics D: Applied Physics* **43,** 264005 (2010).

13. Krawczyk, M. & Grundler, D. Review and prospects of magnonic crystals and devices with reprogrammable band structure. *Journal of Physics: Condensed Matter* **26,** 123202 (2014).

14. Chumak, A. V., Vasyuchka, V. I., Serga, A. A. & Hillebrands, B. Magnon spintronics. *Nature Physics* **11.** Review Article, 453 (2015).

15. Balashov, T., Buczek, P., Sandratskii, L., Ernst, A. & Wulfhekel, W. Magnon dispersion in thin magnetic films. *Journal of Physics: Condensed Matter* **26,** 394007 (2014).

16. Qin, H. J. *et al.* Long-living terahertz magnons in ultrathin metallic ferromagnets. *Nature Communications* **6.** Article, 6126 (2015).

17. Zakeri, K. Probing of the interfacial Heisenberg and Dzyaloshinskii–Moriya exchange interaction by magnon spectroscopy. *Journal of Physics: Condensed Matter* **29,** 013001 (2016).

18. J. Qin, H. *et al.* Magnons in ultrathin ferromagnetic films with a large perpendicular magnetic anisotropy. *Physical Review B* **88** (2013).

19. Chen, Y.-J. *et al.* Group Velocity Engineering of Confined Ultrafast Magnons. *Phys. Rev. Lett.* **119,** 267201 (2017).

20. Sánchez-Barriga, J. *et al.* Effects of spin-dependent quasiparticle renormalization in Fe, Co, and Ni photoemission spectra:An experimental and theoretical study. *Phys. Rev. B* **85,** 205109 (2012).

21. Monastra, S. *et al.* Quenching of Majority-Channel Quasiparticle Excitations in Cobalt. *Phys. Rev. Lett.* **88,** 236402 (2002).

22. Sánchez-Barriga, J. *et al.* Quantitative determination of spin-dependent quasiparticle lifetimes and electronic correlations in hcp cobalt. *Phys. Rev. B* **82,** 104414 (2010).

23. Kzialoshinskii, I. E. The Magnetic Structure of Fluorides of the Transition Metals. *Soviet Journal of Experimental and Theoretical Physics* **6,** 1120 (1958).

24. Moriya, T. Anisotropic superexchange interaction and weak ferromagnetism. *Physical Review* **120,** 91 (1960).

25. Zakeri, K. Probing of the interfacial Heisenberg and Dzyaloshinskii–Moriya exchange interaction by magnon spectroscopy. *Journal of Physics: Condensed Matter* **29,** 013001 (2016).

26. Zakeri, K. *et al.* Asymmetric spin-wave dispersion on Fe (110): direct evidence of the Dzyaloshinskii-Moriya interaction. *Physical review letters* **104,** 137203 (2010).

27. Blundell, S. *Magnetism in Condensed Matter* ISBN: 0198505914 (Oxford University Press, USA, 2001).

28. Kutzelnigg, W. & Morgan, J. D. Hund's rules. *Zeitschrift für Physik D Atoms, Molecules and Clusters* **36,** 197–214. ISSN: 1431-5866 (1996).

29. Simon, S. H. *The Oxford Solid State Basics* ISBN: 0199680779 (Oxford University Press, Usa, 2013).

30. Heisenberg, W. Zur Theorie des Ferromagnetismus. *Zeitschrift für Physik* **49,** 619–636. ISSN: 0044-3328 (1928).

31. Herring, C. Exchange Interactions Among Itinerant Electrons. *Physics Today* **20,** 75 (1967).

32. Zakeri, K. Elementary spin excitations in ultrathin itinerant magnets. *Physics Reports* **545.** Elementary spin excitations in ultrathin itinerant magnets, 47–93. ISSN: 0370-1573 (2014).

33. Stoner, E. C. & Whiddington, R. Collective electron specific heat and spin paramagnetism in metals. *Proceedings of the Royal Society of London. Series A - Mathematical and Physical Sciences* **154,** 656–678 (1936).

34. Stoner, E. C. Collective Electron Ferromagnetism. *Proceedings of the Royal Society of London. Series A, Mathematical and Physical Sciences* **165,** 372–414. ISSN: 00804630 (1938).

35. Wohlfarth, E. P. The Theoretical and Experimental Status of the Collective Electron Theory of Ferromagnetism. *Rev. Mod. Phys.* **25,** 211–219 (1953).

36. Herring, C. & Kittel, C. On the Theory of Spin Waves in Ferromagnetic Media. *Phys. Rev.* **81,** 869–880 (1951).

37. Keffer, F., Kaplan, H. & Yafet, Y. Spin Waves in Ferromagnetic and Antiferromagnetic Materials. *American Journal of Physics* **21,** 250–257 (1953).

38. Dyson, F. J. General Theory of Spin-Wave Interactions. *Phys. Rev.* **102,** 1217–1230 (1956).

39. Sinclair, R. N. & Brockhouse, B. N. Dispersion Relation for Spin Waves in a fcc Cobalt Alloy. *Phys. Rev.* **120,** 1638–1640 (1960).

40. Etzkorn, M., Kumar, A., Vollmer, R., Ibach, H. & Kirschner, J. Spin waves in ultrathin Co-films measured by spin polarized electron energy loss spectroscopy. *Surface Science* **566,** 241–245 (2004).

41. *Lattice constants of the elements* https://periodictable.com/Properties/A/LatticeConstants.wt.html. Accessed: 08. august 2019.

42. Ibach, H. *Physics of Surfaces and Interfaces* ISBN: 3540347097 (Springer, 2006).

43. Chen, Y.-j. *Confined Magnon Modes and Anisotropic Exchange Interaction in Ultrathin Co Films* ISBN: 3832544704 (Logos Verlag Berlin, 2017).

44. Feynman, R. P., Leighton, R. B. & Sands, M. *The Feynman Lectures on Physics, Vol. 3* ISBN: 0201021188 (Addison Wesley, 1971).

45. Zhang, Y. *High wave vector spin waves in ultrathin Fe films on W(110) studied by spin-polarized electron energy loss spectroscopy* PhD thesis (Martin-Luther-Universität Halle-Wittenberg, 2008).

46. Noether, E. Invariante Variationsprobleme. ger. *Nachrichten von der Gesellschaft der Wissenschaften zu Göttingen, Mathematisch-Physikalische Klasse* **1918,** 235–257 (1918).

47. Chan, W.-Y., Tsai, D.-C., Chen, W.-H., Chang, C.-H.-T. & Tsay, J. Enhancement of the polar coercive force for annealed Co/Ir(111) ultrathin films. *Journal of the Korean Physical Society* **62** (2013).

48. Carlomagno, I. *et al.* Co-Ir interface alloying induced by thermal annealing. *Journal of Applied Physics* **120,** 195302 (2016).

49. Lewis, E., Faraday, M., Kerr, J. & Zeeman, P. *The Effects of a Magnetic Field on Radiation: Memoirs by Faraday, Kerr, and Zeeman Scientific memoirs, VIII* **v. 8** (American book Company, 1900).

50. Oakberg, T. C. Magneto-optic Kerr effect. *Hinds Instruments* **1** (2005).

51. Wódkiewicz, K. Classical and quantum Malus laws. *Phys. Rev. A* **51,** 2785–2788 (1995).

52. Auger, P. Sur l'effet photoélectrique composé. *Journal de Physique et le Radium* **6,** 205–208 (1925).

53. Lander, J. Auger peaks in the energy spectra of secondary electrons from various materials. *Physical Review* **91,** 1382 (1953).

54. Davis, L. E., MacDonald, N. C., Palmberg, P. W., Riach, G. E. & Weber, R. E. *Handbook of Auger Electron Spectroscopy: A Reference Book of Standard Data for Identification and Interpretation of Auger Electron Specteroscopy Data* (Physical Electronics Industries, Incorporated, 1976).

55. Pierce, D. T. & Meier, F. Photoemission of spin-polarized electrons from GaAs. *Phys. Rev. B* **13,** 5484–5500 (1976).

56. Drescher, P., Andresen, H. & Aulenbacher, K. Photoemission of spinpolarized electrons from strained GaAsP. *Springer-Verlag* (1996).

57. Mamaev, Y. A. *et al.* Optimized photocathode for spin-polarized electron sources. *Applied Physics Letters* **93,** 081114 (2008).

58. Pratzer, M. & Elmers, H. Structural and magnetic properties of Co-Fe binary alloy monolayers on W (110). *Physical review letters* **90,** 077201 (2003).

59. Ho, H.-Y., Tsay, J.-S. & Chen, Y.-S. Oxygen Adsorption and Magnetic Properties of Ultrathin Co/Ir(111) Films. *Japanese Journal of Applied Physics* **49,** 075802 (2010).

60. Vojta, T., Kotabage, C. & Hoyos, J. A. Infinite-randomness quantum critical points induced by dissipation. *Phys. Rev. B* **79,** 024401 (2009).

61. Schneider, C. M. *et al.* Curie temperature of ultrathin films of fcc-cobalt epitaxially grown on atomically flat Cu(100) surfaces. *Phys. Rev. Lett.* **64,** 1059–1062 (1990).

62. Valvidares, S. M., Dorantes-Dávila, J., Isern, H., Ferrer, S. & Pastor, G. M. Interface-driven manipulation of the magnetic anisotropy of ultrathin Co films on Pt(111): Substrate deposition of hydrogen and model calculations. *Phys. Rev. B* **81,** 024415 (2010).

63. Ibach, H. *Electron Energy Loss Spectroscopy and Surface Vibrations* ISBN: 0123693500 (Academic Pr, 1982).

64. Wiesendanger, R. & Güntherodt, H.-J. *Scanning tunneling microscopy III: theory of STM and related scanning probe methods* (Springer Science & Business Media, 2013).

Acknowledgements

I am very grateful that I got the opportunity to pursue my master thesis at the SPEELS lab. It has been a pleasure to get familiar with this field of study and to be part of the Heisenberg Spin-dynamics group at KIT for one year.

A special thanks must be given to PD Khalil Zakeeri Lori that has been a very dedicated and patient tutor. Thank you for all the interesting discussions, your proofreading, and your support during the work with this thesis. I have learned a lot from you.

I would also like to thank Sergey Tsurkan for teaching me everything about the lab and for always being there to answer my questions. You have made the physics alive, but you also gave life and enjoyable company to the long days at the lab. Thank you for your good mood and singing abilities.

I am thankful to Prof. Dr. Matthieu Le Tacon for being the second referee of my thesis.

I would also like to thank my home university NTNU, for giving me the opportunity to do my master at KIT. A special thanks to Dr. Jon Andreas Støvneng for being my supervisor at NTNU.

Thank you Janek, Sakineh and Sergey for your company and support. The office has always been nice place thanks to you.

I want to thank Marius Jakoby, my boyfriend, for being patient and supportive throughout the year, and for proofreading the thesis.

Last but no least, I want to thank my family back in Norway, for their constant support throughout my studies.